

Understanding and controlling the morphological complexity of biomembranes

Reinhard Lipowsky*

Theory and Bio-Systems, Max Planck Institute of Colloids and Interfaces, Golm, Potsdam, Germany

*Corresponding author: E-mail: Reinhard.Lipowsky@mpikg.mpg.de

Contents

1. Introduction	106
2. Reminder about curvature elasticity	109
3. Fine-tuning the spontaneous curvature	115
4. Composite nature of membrane tension	117
5. Fluid-elastic behavior of planar bilayers	121
6. Shape transformations of nanovesicles	134
7. Two-sphere vesicles and membrane necks	140
8. Curvature-induced division of giant vesicles	146
9. Multispherical shapes of vesicles	148
10. Summary and outlook	153
Acknowledgments	154
References	155

Abstract

Biomimetic and biological membranes consist of lipid-protein bilayers in their fluid state. Because of their fluidity, these membranes can remodel both their molecular composition and their morphology in response to changes in their aqueous environments. Here, we will focus on morphological responses, motivated by recent experimental observations on giant vesicles. After a short reminder about curvature elasticity, two important recent developments will be described, the fine-tuning of the spontaneous curvature by membrane-bound proteins and the increased robustness of giant vesicles with spontaneously formed membrane nanotubes. The latter feature is intimately related to the concept of spontaneous membrane tension, which represents the intrinsic tension scale of curvature elasticity. Another important quantity, the mechanical membrane tension, is, in general, elusive to experimental studies of giant vesicles but can be determined in a quantitative manner by molecular simulations. One recent insight from such simulations is that it is important to distinguish

tensionless bilayers from tensionless leaflets. In addition, using the stress profile obtained in the molecular simulations, we can obtain estimates for the curvature-elastic parameters. In the last part of the review, the framework of curvature elasticity is again taken up to further elucidate the morphological complexity of giant vesicles. Three aspects will be addressed: the stability of two-sphere vesicles with closed membrane necks; the curvature-induced constriction force acting on these necks, which can be used to cleave the necks and divide the vesicles in a controlled manner; and the striking polymorphism of multispheres generated by aqueous sucrose and glucose solutions.



1. Introduction

All biological membranes are organized according to the same universal principle: their basic building block is provided by a bilayer of lipid molecules. These lipid bilayers are maintained in a *fluid* state, which enables the membranes to remodel both their shape and composition in response to changes in their aqueous environment. The diverse responses of biological membranes can be studied, in a systematic manner, using biomimetic membranes with a relatively small number of molecular components [1–3]. From an experimental point of view, particularly useful model systems are provided by giant unilamellar vesicles (GUVs) that have linear dimensions of many micrometers and consist of a single molecular bilayer with a thickness of a few nanometers.

Recent experimental studies have revealed a striking variety of GUV shapes including multisphere or ‘multiballoon’ morphologies, see Fig. 1. One intriguing example for the remodeling of membrane shape is provided by the formation of membrane necks, narrow hourglass-shaped membrane segments that connect two membrane compartments in a continuous manner as shown in Fig. 1A.¹ In the context of cell biology, the formation of such membrane necks represents a crucial step for all endo- and exocytotic processes as well as cell division. The vesicle shape in Fig. 1A involves only one membrane neck. Vesicles can also form multispherical shapes consisting of several spherical compartments. One example is shown in Fig. 1B in which the GUV formed a shape consisting of one large sphere and 14 small ones with the same diameter. Yet another example is provided by

¹ It is amusing to note that membrane necks could also be called ‘wormholes’ in space, providing a loose analogy to the ‘wormholes’ in space-time that have tickled the imagination of science fiction writers.

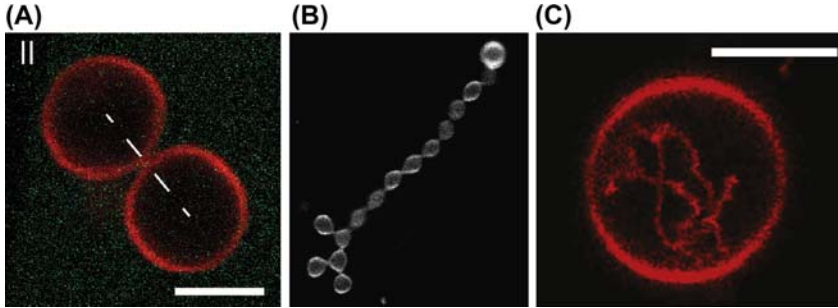


Fig. 1 Striking polymorphism of giant unilamellar vesicles (GUVs): (A) Symmetric dumbbell with a stable membrane neck, prior to fission. The neck formation is induced by the binding of His-tagged proteins to the outer leaflet of the vesicle membrane. Scale bar: $5\ \mu\text{m}$ [5]; (B) Branched multisphere with one large sphere (upper right corner) and 14 small spheres connected by 14 membrane necks. The vesicle membrane is exposed to an interior sucrose and an exterior glucose solution. The large sphere has a diameter of about $3.6\ \mu\text{m}$ [6]; (C) Membrane nanotube protruding from the spherical mother vesicle (red circle) toward the vesicle interior. The nanotube has a width of about $100\ \text{nm}$ and is only visible because the membrane is fluorescently labeled by a red dye. The nanotube forms because the membrane adapts its shape to the large spontaneous curvature which is generated by different lipid compositions of the two bilayer leaflets. Scale bar: $10\ \mu\text{m}$ [7].

membrane nanotubes, highly curved membrane structures that protrude from GUV membranes as in Fig. 1C.

In all examples displayed in Fig. 1, the GUV shapes are determined by the interplay of local bilayer asymmetry of the vesicle membrane arising from molecular interactions and global constraints acting on the membrane area and the vesicle volume [4]. The last couple of years have seen much progress in our understanding of this interplay which will be reviewed in this paper, combining results from molecular simulations, experimental observations, and analytical theory. Indeed, we believe that a real understanding of biomembranes can only be achieved through the integration of theory, simulation, and experiment.

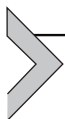
This review is organized as follows. We start with a reminder about the curvature elasticity of biomembranes which also serves to introduce the basic terminology and notation that will be used throughout the paper. Thus, in this introductory section, we explain our convention for the sign of membrane curvature and introduce the curvature-elastic and geometric parameters that determine the membrane morphology. For simplicity, we will focus on uniform membranes with a laterally uniform composition and study their behavior in the framework of the spontaneous curvature model. In the latter

case, the membrane behavior is determined by only two curvature-elastic parameters, the bending rigidity and the spontaneous curvature, and the morphology diagram of the vesicles depends only on two dimensionless shape parameters, the rescaled spontaneous curvature and the volume-to-area ratio. Next, we will address an important recent developments which allows us to fine-tune the spontaneous curvature by membrane-bound proteins in the dilute regime [5]. Another recent insight is related to the concept of the spontaneous tension [8] which leads to an increased robustness of GUVs with spontaneously formed membrane nanotubes [7]. We will also emphasize that the mechanical tension of GUVs is often not accessible to experiment because it is typically rather small and depends on many parameters including the shape and the size of the vesicles.

This experimental difficulty provides one motivation to study the fluid-elastic behavior of lipid bilayers by molecular simulations. We will consider both planar bilayers [9–11] and spherical nanovesicles [12], which have a diameter of about 45 nm and undergo a striking variety of shape transformations, qualitatively similar to those observed for GUVs on the micrometer scale. Both for planar bilayers and for nanovesicles, we will discuss the underlying pressure tensor and stress profile. Using these stress profiles, we can determine both tensionless bilayers and tensionless leaflets, which are both important to describe the fluid-elastic behavior of the bilayers. Furthermore, we also emphasize that we can deduce the curvature-elastic parameters from the molecular simulations, thereby providing a direct connection between the molecular and the curvature-elastic or nanoscopic view of the membranes.

In the last part of the review, we return to the curvature-elastic view, starting with a detailed analysis of dumbbell shapes or two-sphere vesicles consisting of two spherical membrane segments that are connected by a closed, hourglass-shaped membrane neck as in Fig. 1A. In fact, the shape of this neck cannot be resolved in Fig. 1A because of the limited optical resolution but such dumbbell shapes with membrane necks have also been observed in nanovesicle simulations and confirm our naive expectations that the neck diameter is about twice the bilayer thickness, i.e., of the order of 10 nm. Understanding the curvature elasticity of two-sphere spheres will enable us to address the two last topics: (i) the curvature-induced cleavage of membrane necks and the concomitant division of vesicles into two daughter vesicles; and (ii) the striking variety of multisphere or multiballoon morphologies. At the end, I will summarize the main theoretical and experimental

results and will give a brief outlook on the many challenging questions to be addressed in future studies.



2. Reminder about curvature elasticity

Membranes as smoothly curved surfaces. In Fig. 1, the GUV membranes are visible as thin and smoothly curved cross sections. Thus, in this section, we will ignore the detailed molecular architecture of the membranes and view them as smoothly curved surfaces or sheets, which are governed by their bending rigidity κ , which provides the basic energy scale, and their spontaneous (or preferred) curvature m , which represents an inverse length scale. The bending rigidity κ was originally introduced in the context of elastic membrane models for red blood cells and giant vesicles [13–15] but is, in fact, a meaningful concept down to molecular scales as revealed by molecular dynamics simulations [16]. The spontaneous curvature m is a quantitative measure for the intuitive notion that a membrane may prefer to bend toward one side rather than toward the other, reflecting some asymmetry between its two sides. The spontaneous curvature was originally discussed by Bancroft for surfactant monolayers in water–oil emulsions [17,18] and was included by Frank as the so-called ‘splay term’ in the curvature elasticity of liquid crystals [19]. In the context of lipid bilayers, spontaneous curvature was first introduced by Helfrich [14]. The corresponding curvature energy of the membrane is now known as the spontaneous curvature model [20].

The spontaneous curvature model implicitly assumes that the area difference between the two leaflets can change via flip-flops of lipid molecules. While a phospholipid molecule may stay in the same leaflet for hours or even days [21–23], cholesterol or other sterols flip-flop from one leaflet to the other within seconds [24,25] or even milliseconds [26]. Therefore, it is plausible that the spontaneous curvature model provides a reliable description for bilayer membranes that contain at least one flip-flopping species such as cholesterol, as proposed some time ago [27]. This conjecture has now been confirmed by two recent experimental studies of GUVs [5,6] which contained a certain mole fraction of cholesterol in their membranes and attained the remarkable shapes displayed in panel A and B of Fig. 1.

If all membrane components undergo very slow flip-flops, the number of molecules is essentially fixed within each leaflet and the quenched difference between these two numbers leads to a preferred area difference

between the leaflets. This constraint was originally considered by Evans [15], incorporated into the bilayer-coupling model of Svetina and Zeks [20,28], and generalized in terms of the area-difference-elasticity model [29–31]. In the following, we will focus on the spontaneous curvature model.

Sign convention about the membrane curvature. At each point of a smoothly curved membrane, the local membrane shape can be described in terms of its principal curvatures, C_1 and C_2 , which define the mean curvature M and the Gaussian curvature G via

$$M \equiv \frac{1}{2}(C_1 + C_2) \quad \text{and} \quad G = C_1 C_2. \quad (1)$$

It is important to note that the two principal curvatures as well as the mean and Gaussian curvatures can be positive or negative and that these signs involve a certain convention. Here and below, we will use the sign convention that the mean curvature M is *positive* if the membrane bulges locally toward the exterior compartment, see Fig. 2A. Likewise, M is taken to be *negative* if the membrane bulges locally toward the interior compartment as in Fig. 2C. The sign convention for M is intimately related to the choice for the normal vector of the membrane surface. The convention used here implies that this normal vector is always chosen to point toward the exterior compartment.

Spontaneous curvature model. We now focus on membranes that have a uniform composition which implies that they have laterally uniform curvature-elastic properties as described by constant bending rigidity κ and spontaneous curvature m . Following the sign convention for the mean curvature, see Fig. 2, the spontaneous curvature m is taken to be positive and negative if the membrane prefers to bulge towards the exterior and interior

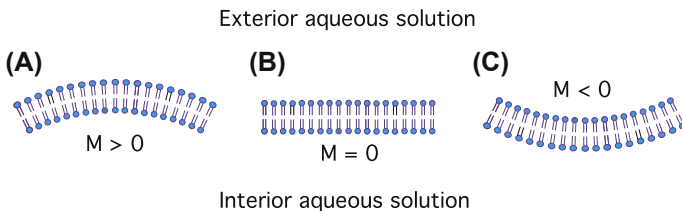


Fig. 2 Sign convention for mean curvature M : (A) The mean curvature is *positive* if the membrane bulges locally toward the exterior aqueous solution; (B) The mean curvature vanishes for a planar membrane; and (C) The mean curvature is *negative* if the membrane bulges locally toward the interior solution. The expression ‘bulges toward’ is used here because it is less ambiguous than the expressions ‘bends toward’ or ‘curves toward’.

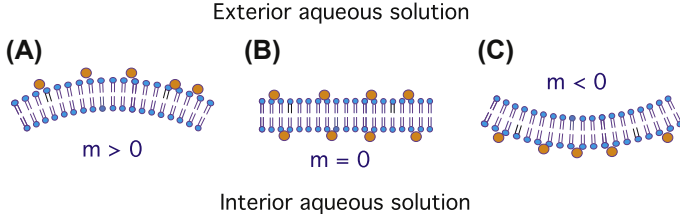


Fig. 3 Sign convention for spontaneous curvature m : (A) The spontaneous curvature is *positive* if the membrane prefers to bulge toward the exterior compartment; (B) The spontaneous curvature vanishes if the membrane prefers to remain planar; and (C) The spontaneous curvature is *negative* if the membrane prefers to bulge locally toward the interior compartment. This sign convention for m is imposed by the sign convention for M in Fig. 2. In the cartoons, the spontaneous curvature is generated by the asymmetric binding of small solutes to the leaflets of the bilayer membrane [8,9,32]. Essentially the same curvature is generated when we replace the solutes by lipids with large head groups [10].

compartment, respectively, as in Fig. 3. Within the spontaneous curvature model, we keep all terms up to second order in the principal curvatures C_1 and C_2 which leads to the curvature energy [4,14,20].

$$E_{\text{cu}} = E_{\text{be}} + \kappa_G \int dA G \quad (2)$$

with the bending energy

$$E_{\text{be}} = 2\kappa \int dA (M - m)^2 \quad (3)$$

where the area integrals extend over the whole membrane surface. The bending energy E_{be} vanishes for $M = m$, i.e., when the whole membrane adapts its mean curvature M to the spontaneous curvature m . In general, such an adaptation is not possible, however, since the membrane experiences additional constraints arising, in particular, from the vesicle volume and the membrane area. The additional energy term proportional to the area integral over the Gaussian curvature G does not depend on the membrane shape as long as we consider membranes with a laterally uniform composition and without membrane edges, as follows from the Gauss-Bonnet theorem. In the following, these two conditions will always be fulfilled apart from the section on the curvature-induced fission.

Typical values of the curvature-elastic parameters. The bending energy of a fluid membrane as described by Eq. (3) depends only on two curvature-elastic parameters, the bending rigidity κ and the spontaneous

curvature m . The bending rigidity κ has the dimension of an energy with a typical value of the order of $20 k_B T$ or 10^{-19} J for lipid membranes. For the GUV membrane in Fig. 1A, which contained a ternary mixture of POPC, POPG, and cholesterol, the rigidity was measured to be $\kappa = 48 k_B T$ [5]. For the GUV membrane in Fig. 1C, consisting of a binary mixture of POPC and 4 mol% of the glycolipid (or ganglioside) GM1, the rigidity was about $\kappa = 20 k_B T$ [7,33]. The bending rigidity can be measured by a variety of experimental methods, recently reviewed in Ref. [34].

While the bending rigidities of different lipid membranes typically differ only by a factor of two to four, the spontaneous curvatures can vary over several orders of magnitude. The GUV membrane in Fig. 1A, for example, had a *positive* spontaneous curvature $m = 1.45 \mu\text{m}^{-1} = 1/(690 \text{ nm})$ induced by the binding of His-tagged protein to the outer leaflet of the membrane (corresponding to a solution concentration $X = 7.8 \text{ nM}$ and 0.1 mol% anchor lipids) [5]. The GUV membrane that formed the in-ward pointing nanotube in Fig. 1C, on the other hand, had the *negative* spontaneous curvature $m = -10.5 \mu\text{m}^{-1} = -1/(95 \text{ nm})$ arising from an asymmetric composition of the two leaflets [7].

Volume and area as important shape parameters. The vesicle volume is primarily determined by the osmotic conditions and the temperature. Therefore, one convenient procedure to change the vesicle volume at constant temperature is via osmotic inflation and deflation. Osmotic deflation is limited by the attractive intermolecular forces that start to become important when different membrane segments come into close proximity. Thus, at very small volumes, different segments of the vesicle membrane may start to fold back onto themselves or to form local membrane stacks. On the other hand, osmotic inflation is limited by the available membrane area. Indeed, for a given membrane area A and the corresponding vesicle size

$$R_{\text{ve}} \equiv \sqrt{A/(4\pi)}, \quad (4)$$

the vesicle volume V attains its maximal value when the vesicle has a spherical shape. Therefore, for constant membrane area A , the vesicle volume satisfies the inequality

$$V \leq \frac{4\pi}{3} R_{\text{ve}}^3 = \frac{4\pi}{3} \left(\frac{A}{4\pi} \right)^{3/2}. \quad (5)$$

For constant temperature and lipid composition, the area A of the vesicle membrane is primarily determined by the number of lipid molecules within

the membrane. Indeed, in the absence of external forces or constraints, the lipids attain a certain molecular area corresponding to their optimal packing density. In principle, the membrane area can be changed by a mechanical tension that acts to stretch the membrane. However, nonspherical shapes as in Fig. 1 are always characterized by a mechanical tension that is several orders of magnitude smaller than the area compressibility modulus of the membrane which implies that the area dilation of the GUV membrane is very small, see Eq. (14) further below. On the other hand, for GUVs, one can directly measure the vesicle volume V and the membrane area A . It is therefore rather natural from an experimental point of view to regard V and A as basic geometric parameters that determine the vesicle shape.

Dimensionless shape parameters and morphology diagram.

From the previous discussion, we can conclude that the shape of a GUV depends on four parameters, the bending rigidity κ and the spontaneous curvature m , which represent two curvature-elastic material parameters, as well as the vesicle volume V and the membrane area A , which determine the overall dimensions of the vesicle. It is now convenient to choose the bending rigidity κ as the basic energy scale and the vesicle size $R_{\text{ve}} = \sqrt{A/(4\pi)}$ as the basic length scale. As a consequence, the dimensionless bending energy E_{be}/κ depends only on two dimensionless shape parameters [20]. The first such parameter is provided by the volume-to-area ratio (also known as the ‘reduced volume’)

$$v = \frac{V}{\frac{4\pi}{3}R_{\text{ve}}^3} = \frac{6\sqrt{\pi}V}{A^{3/2}} \quad \text{which satisfies } 0 < v \leq 1. \quad (6)$$

A single sphere is described by $v = 1$, in accordance with the inequality for the volume V in Eq. (5). The second dimensionless shape parameter is given by the dimensionless spontaneous curvature

$$\bar{m} = mR_{\text{ve}} = m\sqrt{A/(4\pi)}. \quad (7)$$

Any vesicle shape can now be specified in terms of the two shape parameters v and \bar{m} . To simplify the following discussion, we will focus on zero or positive values of the spontaneous curvature and, thus, on $\bar{m} \geq 0$. The resulting morphology diagram is then provided by the semi-infinite (\bar{m}, v) -strip with $\bar{m} \geq 0$ and $0 < v \leq 1$.

This morphology diagram has been theoretically explored in some detail for relatively small values of the spontaneous curvature \bar{m} with $|\bar{m}| \leq 2$ [20]. In this regime, the vesicle can typically form only a few (meta)stable shapes

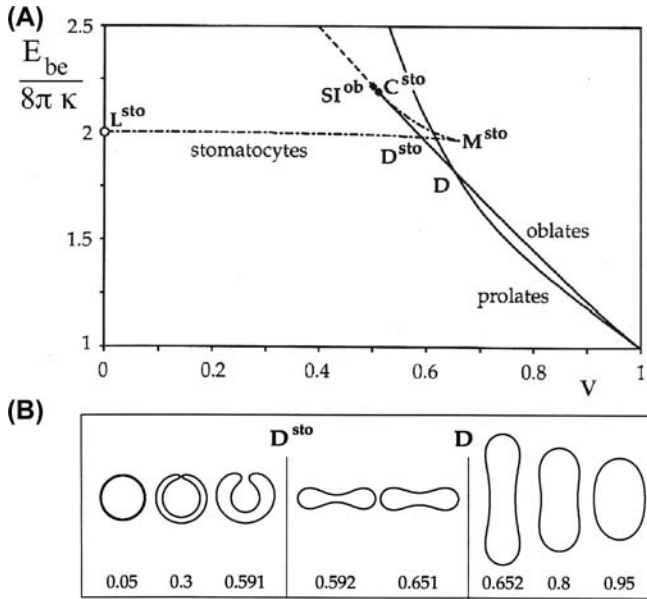


Fig. 4 Shapes of vesicles that minimize the bending energy of their membranes for zero spontaneous curvature: (A) Dimensionless bending energy $E_{be}/(8\pi\kappa)$ as a function of volume-to-area ratio ν for spontaneous curvature $m = 0$. The sphere is obtained for $\nu = 1$. The different lines correspond to different branches of (meta)stable states. For small ν , we obtain the limit shape L^{sto} of a stomatocyte consisting of two nested spheres connected by a membrane neck, see leftmost shape in the bottom row; and (B) Corresponding vesicle shapes for different values of ν (digits in the bottom line) as obtained for constant area A and variable volume V [20]. (with permission).

for a certain point (\bar{m}, ν) in the morphology diagram. This situation is illustrated in Fig. 4 by the branches of the bending energy for zero spontaneous curvature as a function of ν . [20] However, these theoretical results for the GUV morphology have been difficult to scrutinize by experiment, basically for two reasons. First, many experimental studies in the 1990s looked at bilayers of phospholipids that did not flip-flop from one leaflet of the bilayer membrane to the other on the time scales of the experiments. In such a situation, the number of lipids remains constant within each leaflet which implies an additional constraint on the area-difference between the two leaflets, which leads to another contribution of the bending energy [29–31]. The latter contribution is, however, nonlocal and involves another curvature-elastic parameter. This complication can be avoided if one studies lipid membranes that contain cholesterol or other sterol molecules, which undergo frequent flip-flops between the bilayer leaflets, as explicitly

demonstrated by two recent experimental studies [5,6]. Second, it has not been possible, until quite recently, to experimentally control the (local) spontaneous curvature m , which defines the spontaneous curvature model, in a systematic and reliable manner. The latter obstacle has now been overcome by the experimental approach described in the next section. This new approach should also allow us to explore the morphology diagram for larger values of \bar{m} . In the latter regime, we expect to find an increased number of (meta)stable energy branches as indicated by the large variety of multispherical shapes [4,6,35] that will be discussed further below.



3. Fine-tuning the spontaneous curvature

During the last couple of years, a variety of methods has been developed to determine the spontaneous curvature of GUV membranes by a detailed theoretical analysis of the observed GUV shapes [7,36,37]. What has been missing, however, was an experimental protocol that allowed us to vary the spontaneous curvature in a controlled and quantitative manner. Such a protocol has now been developed based on the reversible binding of His-tagged GFP proteins to anchor-lipids within the GUV membranes [5].

Coverage of outer leaflet by membrane-bound GFP. The proteins were added to the exterior aqueous solution of the GUVs, which led to a certain coverage of the outer leaflet by membrane-bound GFP, depending on the mole fraction of the anchor-lipids. By calibrating the fluorescence of the membrane-bound proteins, the GFP coverage Γ of the membranes was shown to increase linearly with the protein solution concentration X according to

$$\Gamma = \frac{69}{\mu\text{m}^2} \frac{X}{\text{nM}} \quad \text{for 1 mol\% anchor - lipids} \quad (8)$$

over the concentration range $0 < X \leq 23.4$ nM. The GFP concentration $X = 23.4$ nM leads to the GFP coverage $\Gamma = 1615 \mu\text{m}^{-2}$ and an average GFP-GFP separation of 25 nm. For 0.1 mol% anchor-lipids, the prefactor 69 in Eq. (8) is reduced to 6.9. The largest GFP concentration to which we exposed the GUVs with 0.1 mol% anchor-lipids was $X = 39$ nM which led to the GFP coverage $\Gamma = 269 \mu\text{m}^{-2}$, corresponding to an average separation of 61 nm between the membrane-bound GFPs.

For all concentrations, the average separation of the lipid-anchored GFPs exceeded 24 nm, which is much larger than the GFP's lateral size of about 3 nm [38]. As a consequence, the whole concentration range explored here

belongs to the dilute regime in which we can ignore steric interactions between the membrane-bound molecules or as well as protein crowding effects, which have been studied in Refs [39, 40].

Spontaneous curvature proportional to GFP coverage. As we increased the GFP concentration X and, thus, the GFP coverage Γ of the outer membrane leaflet, the two sides of the membranes became more and more asymmetric, generating a preferred or spontaneous curvature that increased with Γ . Furthermore, a detailed comparison between theory and experiment also revealed that the spontaneous curvature m generated by this bilayer asymmetry increased linearly with the GFP coverage Γ and the GFP solution concentration X according to

$$m = \Gamma \times 27 \text{ nm} = \frac{\alpha}{\mu\text{m}} \frac{X}{\text{nM}} \quad (9)$$

with the prefactor $\alpha = 0.186$ for 0.1 mol% and $\alpha = 1.86$ for 1 mol% anchor-lipids.

The spontaneous curvature m generated by lipid-anchored GFP is surprisingly large as can be seen when we compare it with the spontaneous curvature generated by membrane-bound amphiphysin, which is a BAR-domain protein. For the latter protein, tube-pulling experiments were used [41] to estimate the spontaneous curvature. In the dilute regime, three different estimates were obtained. When we express these estimates in the form of Eq. (9), we obtain the amphiphysin-generated spontaneous curvature $m = \Gamma L_m$ with the length scale L_m given by 10 nm, 25 nm, and 50 nm, respectively, which should be compared to the value $L_m = 27$ nm as obtained here for GFP. Therefore, the spontaneous curvature generated by lipid-anchored GFP is certainly comparable in size to the one generated by membrane-bound amphiphysin and may even be three times larger.

Exploring the morphology diagram of GUVs. Using the fine-tuning of the spontaneous curvature m via the GFP concentration as described in the previous paragraphs, we can now start to scrutinize the morphology diagram of GUVs in a systematic and detailed manner. Indeed, for uniform membranes, this morphology diagram depends only on the spontaneous curvature $\bar{m} = mR_{ve}$ and on the volume-to-area ratio v , and the latter shape parameter is easily changed by changes in the osmotic conditions. This increased control over the shape is illustrated in Fig. 5 for three GFP concentrations. Inspection of this figure directly shows that the GUV membranes try to adapt to the increased GFP coverage by forming more highly curved shapes.

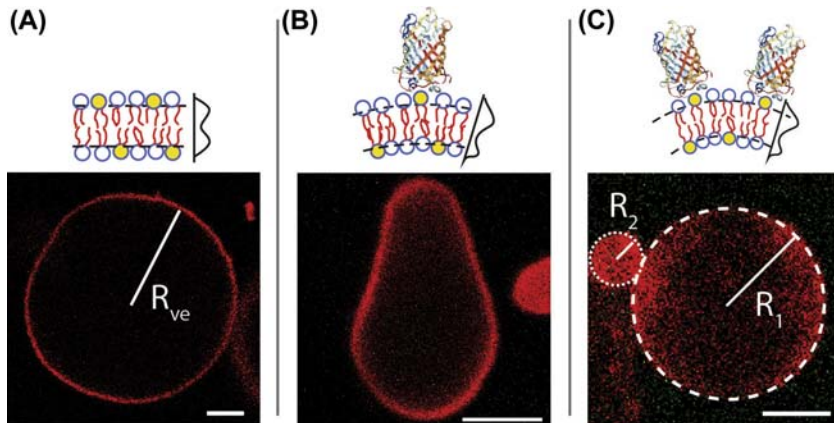


Fig. 5 Curvature of GUV membranes (red) induced by His-tagged GFP: (A) in the absence of GFP; (B) for GFP solution concentration $X = 0.78$ nM and GFP coverage $\Gamma = 5.4 \mu\text{m}^{-2}$ as well as (C) for $X = 7.8$ nM and $\Gamma = 54 \mu\text{m}^{-2}$. In the cartoons, the anchor-lipids (yellow) bind the HIS-tags of the bulky GFP barrels (multi-colored). These protein barrels have an extension that is comparable to the lipid bilayer thickness of about 4 nm. The average separation of the membrane-bound GFPs is, however, not drawn to scale, and about 136 nm in (C). The leftmost image displays a spherical GUV with vesicle size $R_{ve} \equiv \sqrt{A/(4\pi)} = 14.5 \mu\text{m}$. The rightmost image shows a dumb-bell shape consisting of two spherical membrane segments with radii $R_1 = 8.4 \mu\text{m}$ and $R_2 = 2.6 \mu\text{m}$. All scale bars: $5 \mu\text{m}$ [5].



4. Composite nature of membrane tension

Shape equations for cylinders and spheres. When we minimize the bending energy of the spontaneous curvature, we obtain a shape equation [42] that is, in general rather, difficult to solve. For spherical and cylindrical membrane segments, the shape equations reduce to polynomial equations in the constant mean curvature of the respective shapes. In fact, the shape equation always contains a term that is linear in the mean curvature with a prefactor that has the form [4,8].

$$\widehat{\Sigma} \equiv \Sigma + 2\kappa m^2. \quad (10)$$

The first term represents the mechanical membrane tension Σ whereas the second term, $2\kappa m^2$, can be interpreted as another type of tension, the so-called spontaneous tension. The two terms have a very different character because the mechanical tension arises from the external constraints and forces acting on the membrane whereas the spontaneous tension depends

only on the curvature-elastic parameters κ and m . These two types of different tensions will now be discussed in more detail.

Spontaneous membrane tension. The bending energy of the spontaneous curvature model as given by Eq. (3) depends only on two curvature-elastic parameters, the bending rigidity κ and the spontaneous curvature m . The only tension scale that can be defined, apart from a multiplicative factor, by these two parameters is the spontaneous tension [8]

$$\sigma \equiv 2\kappa m^2, \quad (11)$$

which represents the intrinsic tension of curvature elasticity. The spontaneous tension determines the bending energy of a membrane segment that has a significant spontaneous curvature but is forced to remain weakly curved with mean curvature $M \simeq 0$ by external constraints arising, e.g., from osmotic inflation. Indeed, if such a membrane segment has the area A , its bending energy is $\sigma A = 2\kappa m^2 A$. Furthermore, when the membrane has a bending rigidity of about 10^{-19} J, a spontaneous curvature of $1/(20 \mu\text{m})$ leads to a spontaneous tension of about 10^{-6} mN/m while a spontaneous curvature of $1/(20 \text{nm})$ leads to a spontaneous tension of about 1 mN/m. Thus, in real membrane systems, the spontaneous tension can vary over six orders of magnitude.

The spontaneous membrane tension σ is a material parameter, in contrast to the mechanical membrane tension Σ arising from external forces or constraints. Because the spontaneous tension is proportional to m^2 , a significant spontaneous curvature generates a spontaneous tension that is large compared to the mechanical tension [4,8]. One example is provided by GUVs with spontaneously formed nanotubes, see Fig. 1C, which behave like liquid droplets with a variable surface area and with an effective interfacial tension that is provided by the spontaneous tension σ . This droplet-like behavior, which reflects the area reservoir that the nanotubes provide for the mother vesicle, leads to an increased robustness against mechanical perturbations as has been recently demonstrated by micropipette aspiration and repeated cycles of osmotic deflation and inflation [7]. In the context of micropipette aspiration, a mechanical instability has been observed as schematically shown in Fig. 6. The spontaneous tension will also show up in the context of closed membrane necks as we will see further below.

Mechanical membrane tension. So far, we have focused on the curvature elasticity of the GUV membranes and ignored the possibility that the membrane may be stretched or compressed by mechanical forces. Indeed,

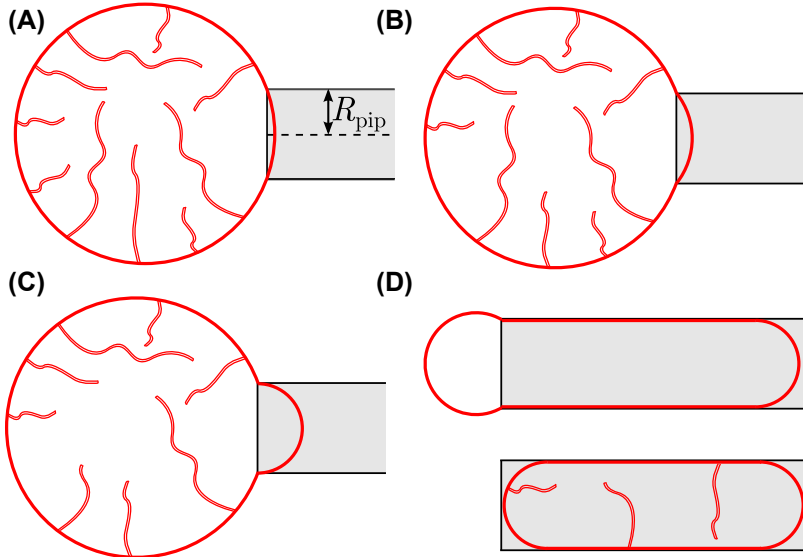


Fig. 6 Droplet-like behavior of a tubulated GUV (red) during micropipette aspiration: (A) The spherical mother vesicle comes into contact with the pipette; (B) With increasing suction pressure, some of the nanotubes are retracted and the mother vesicle develops a tongue that has the form of a spherical cap; (C) When the suction pressure reaches a critical value, the cap-like tongue becomes a hemisphere with radius R_{pip} , mechanical stability is lost, and the vesicle membrane starts to flow into the micropipette; and (D) Depending on the membrane area stored in the nanotubes, the vesicle motion stops as soon as all nanotubes have been retracted (D, top) or continues until the vesicle is completely aspirated into the pipette (D, bottom). In the latter case, the tubulated vesicle behaves as a liquid droplet with an effective interfacial tension that is equal to the spontaneous tension $\sigma = 2 \text{ km}^2$ [7].

the nicely curved GUV shapes displayed in Fig. 1 or Fig. 5 are only possible as long as the vesicle membranes do not experience a significant mechanical tension. A simple way to increase this tension is by osmotic inflation. Thus, if we exposed any of the GUVs in Fig. 1 to an exterior hypotonic solution, water would permeate into the vesicle and increase its volume until the GUV has reached a spherical shape. The latter shape is governed by mechanical membrane tension rather than by curvature elasticity, in close formal analogy to the spherical shape of a liquid droplet.

The mechanical tension Σ acting on a vesicle membrane can be theoretically described in two distinct but equivalent ways [43]. First, we may view the vesicle volume V and the membrane A as two control parameters and minimize the bending energy of the membrane under the constraint that

these two parameters have certain, prescribed values. We are then led to minimize the shape energy [20,44]

$$F = -\Delta PV + \Sigma A + E_{\text{be}} = -\Delta PV + \Sigma A + 2\kappa \int dA(M-m)^2 \quad (12)$$

and to treat the parameters ΔP and Σ as Lagrange multipliers that allow us to perform the constrained minimization of the bending energy. Second, we can consider the stretching energy

$$E_{\text{st}} = \frac{K_A}{2} \frac{(A - A_{\text{opt}})^2}{A_{\text{opt}}} \quad (13)$$

and the associated mechanical tension

$$\Sigma_{\text{mec}} = K_A \frac{A - A_{\text{opt}}}{A_{\text{opt}}} \quad (14)$$

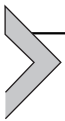
which are both proportional to the area compressibility modulus K_A . The membrane is tensionless when the membrane area has its optimal value, $A = A_{\text{opt}}$. We now minimize the combined bending and stretching energy $E_{\text{be}} + E_{\text{st}}$ for given volume V , using a two-step procedure [43]. We then find that $\Sigma = \Sigma_{\text{mec}}$, i.e., the Lagrange multiplier tension Σ , which ensures that the area has the prescribed value A , is equal to the mechanical tension Σ_{mec} , which was generated by increasing the membrane area from A_{opt} to A . Thus, we do not need to distinguish the two tensions by a different symbol and continue to denote both of them by Σ .

When we view the mechanical membrane tension Σ as a Lagrange multiplier, we can directly conclude that this tension will depend on the size and shape of the vesicle. This can be shown explicitly for multispherical GUV shapes as in Fig. 1A, see Eq. (53) further below. However, so far, we have no reliable method to experimentally measure mechanical membrane tensions of freely suspended vesicles directly, both because these tensions are typically rather small and because their numerical values will change when our tension probe perturbs the membrane shapes.²

On the other hand, the mechanical membrane tension can be studied, in a systematic manner, by molecular simulations of lipid bilayers as we will explain in the next section. One immediate difference to the preceding

² This influence of the measurement process on the tension Σ is reminiscent of the uncertainty principle in quantum mechanics.

sections, which were based on the view that the membranes behave as smoothly curved surfaces, is that we now ‘see’ that the membranes are molecular bilayers that consist of two monolayers or leaflets. In fact, one important insight that has been recently obtained from such simulations is that we need to distinguish the mechanical tension Σ of the whole bilayer from the mechanical tensions of the two bilayer leaflets. In addition, it will also become apparent that we can use molecular simulations to estimate the numerical values of the two curvature-elastic parameters κ and m , thereby providing a direct connection between molecular and nanoscopic or mesoscopic scales.



5. Fluid-elastic behavior of planar bilayers

In the previous section on curvature elasticity, we ignored the molecular structure of the membranes and described them as smoothly curved surfaces. We know, however, that real lipid membranes are molecular bilayers with a thickness of about 4–5 nm. In this and the next section, we now take this bilayer structure into account by molecular modeling and simulations. In the present section, we study planar bilayers with periodic boundary conditions, in the next section, nanovesicles as provided by closed bilayers without any edges.

Emergence of membrane curvature at the nanoscale. The simplest membrane system that can be elucidated by molecular simulations is provided by a planar bilayer that spans the simulation box and is subject to

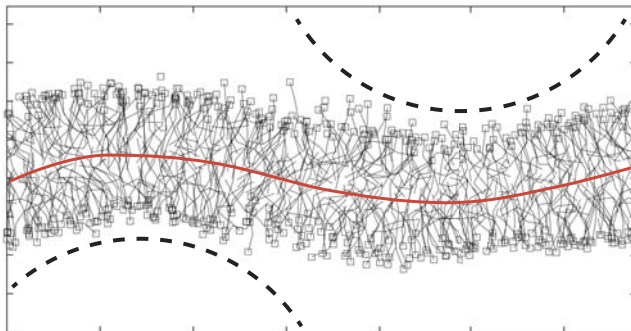


Fig. 7 Emergence of membrane curvature in molecular dynamics simulations of a symmetric and tensionless bilayer [16]. The lipid bilayer has a thickness of about 4 nm, the smallest curvature radius of its midsurface (red) is about 6 nm. For comparison, two circles (broken lines) with a radius of 6 nm are also displayed.

periodic boundary conditions. To determine the curvature–elastic properties of such a bilayer, it has to be prepared in a state of sufficiently low membrane tension as illustrated in Fig. 7 [16]. It is important to note, however, that the description of the membrane shape in terms of curvature requires a certain amount of coarse graining. Indeed, because membranes are immersed in liquid water, each membrane molecule undergoes thermal motion with displacements both parallel and perpendicular to the membrane. The perpendicular displacements represent molecular protrusions that roughen the two interfaces bounding the membrane as in Fig. 7.

Therefore, in order to characterize a lipid–protein bilayer by its curvature, one has to consider small membrane patches and to average over the molecular conformations within these patches. The minimal lateral size of these patches can be determined from the analysis of the bilayer’s shape fluctuations and was found to be about 1.5 times the membrane thickness, as in Fig. 7, for both one–component [9,16] and two–component [10] lipid bilayers. For a membrane with a thickness of 4 nm, this minimal size is about 6 nm. Because such a membrane patch contains 80–100 lipid molecules, membrane curvature should be regarded as an emergent property arising from the collective behavior of a large number of lipid molecules.

Stress profile of planar bilayers. A tensionless bilayer as in Fig. 7 can be obtained by varying the lateral size of the simulation box and measuring the bilayer tension for different sizes. To do so, we consider a bilayer assembled from a certain number of lipids, introduce a Cartesian coordinate system (x, y, z) with the coordinate z being perpendicular to the bilayer, and compute the pressure tensor \mathbf{P} which has the general form

$$\mathbf{P} = P_T(z) \left[\mathbf{e}_x \otimes \mathbf{e}_x + \mathbf{e}_y \otimes \mathbf{e}_y \right] + P_N \mathbf{e}_z \otimes \mathbf{e}_z \quad (15)$$

with the tangential component $P_T(z)$ and the normal component P_N where \mathbf{e}_x , \mathbf{e}_y , and \mathbf{e}_z are orthogonal unit vectors and the symbol \otimes represents the dyadic product. The periodic boundary conditions ensure that the pressure components can depend only on the coordinate z . Furthermore, all components of the divergence of the pressure tensor, which is a vector with the Cartesian components $\sum_j \partial P_{ij} / \partial x_j$, must vanish [45]. In the present context, the latter requirement leads to $\partial P_{zz} / \partial z = 0$ which implies that $P_{zz} = P_N$ does not depend on z and is constant throughout the simulation box.

The tangential and normal components $P_T(z)$ and P_N of the pressure tensor determine the stress profile

$$s(z) \equiv P_N - P_T(z) \quad (16)$$

across the bilayer. Note that positive stress $s > 0$ implies local stretching whereas negative stress $s < 0$ describes local compression. The bilayer tension Σ is finally obtained from the integral [46].

$$\Sigma = \int_{-\infty}^{+\infty} dz s(z). \quad (17)$$

in close analogy to the interfacial tension [45] of planar liquid-liquid interfaces. Both the stress profile and the bilayer tension vary with the lateral size of the simulation box for a fixed number of membrane molecules. Furthermore, the bilayer tension Σ changes sign for a certain lateral box size, which defines the tensionless state of the bilayer [46].

Midplane and leaflet tensions of planar bilayers. A molecular bilayer consists of two leaflets. For a vesicle membrane, it is natural to distinguish an outer from an inner leaflet. For a planar membrane, we will distinguish an upper from a lower leaflet which we take to be in contact with the exterior and interior aqueous solution, respectively. Thus, the upper leaflet of the planar bilayer plays the role of the outer leaflet of the vesicle membrane, and the lower leaflet of the planar bilayer corresponds to the inner leaflet of the vesicle. The properties of the lower leaflet will be labeled by the subscript ‘low’, those of the upper leaflet by the subscript ‘upp’.

To decompose the bilayer tension Σ into separate contributions from the two leaflets, we define a midplane of the planar bilayer and shift the z -coordinate in such a way that the midplane is located at $z = 0$. In contrast to the neutral surface of a bilayer [47,48], the midplane considered here is not defined in terms of elastic deformations or stresses but represents the molecular interface between the two bilayer leaflets. Thus, the midplane is conveniently defined by the individual density profiles of specific molecular groups, such as the hydrocarbon chains or the head groups of the lipids, or by the center-of-mass of the total density profile of the lipids [9–12]. The presumably simplest option is to locate the midplane at the extremum of the density profile $\rho_c(z)$ for the hydrocarbon chains of the lipids. For coarse-grained molecular simulations as used in Refs. [9,10,12], the density profile $\rho_c(z)$ exhibits a pronounced maximum as shown in Fig. 8. For spherical bilayers, a recent study also showed that different definitions of the mid-surface do not change the location of this surface in any significant way [12].

Once the midplane of the planar bilayer has been defined and located at $z = 0$, the bilayer tension Σ can be decomposed into two contributions via

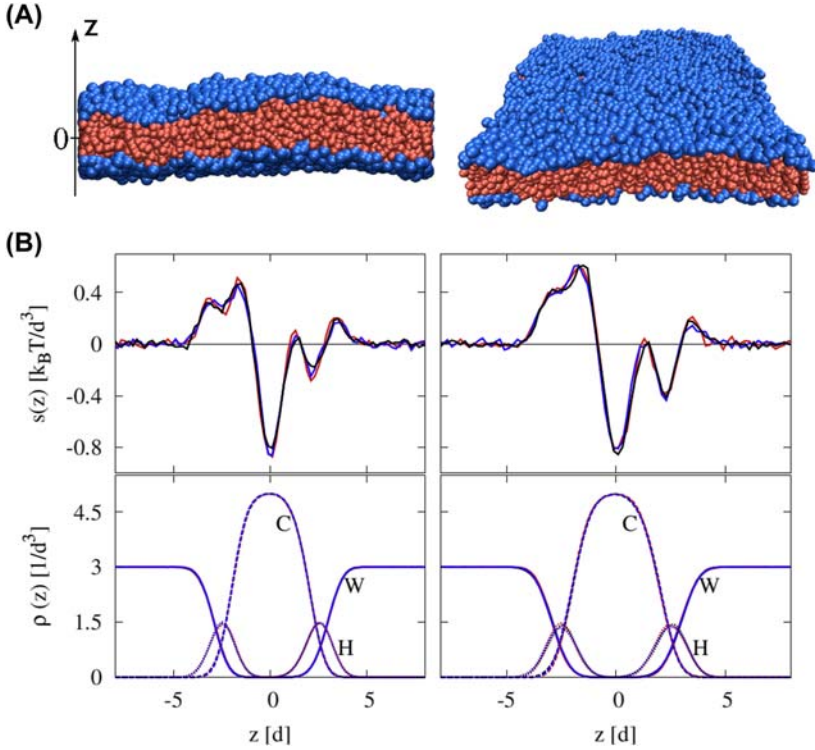


Fig. 8 Asymmetric and tensionless bilayers, assembled from one lipid component with different lipid numbers, N_{upp} and N_{low} , in the upper and lower bilayer leaflets. The resulting bilayer asymmetry is characterized by the mole fraction $\varphi \equiv N_{\text{upp}}/(N_{\text{upp}} + N_{\text{low}})$: (A) Cross section and oblique view of an asymmetric bilayer with $N_{\text{upp}} > N_{\text{low}}$ and $\varphi > 1/2$. The lipids have blue head groups and red hydrocarbon chains. The Cartesian coordinate z perpendicular to the bilayer is measured in units of the bead diameter $d \approx 0.8$ nm; and (B) Stress and density profiles, $s(z)$ and $\rho(z)$, for $\varphi = 0.514$ (left panels) and $\varphi = 0.522$ (right panels). The two φ -values lead to different stress profiles, whereas the density profiles remain practically unchanged. The location of the mid-plane at $z = 0$ is defined by the pronounced and robust peak in the density profile of the chain (C) beads. [9] (with permission)

$$\Sigma = \Sigma_{\text{upp}} + \Sigma_{\text{low}} \quad (18)$$

with the upper and lower leaflet tensions

$$\Sigma_{\text{upp}} \equiv \int_0^{+\infty} dz s(z) \quad \text{and} \quad \Sigma_{\text{low}} \equiv \int_{-\infty}^0 dz s(z). \quad (19)$$

From these definitions, we can immediately conclude that the two leaflet tensions have opposite signs with

$$\Sigma_{\text{low}} = -\Sigma_{\text{upp}} \text{ for tensionless bilayers with } \Sigma = 0. \quad (20)$$

In order to further elucidate the interrelation between leaflet tensions and curvature elasticity, we now distinguish between symmetric and asymmetric bilayers.

Stretching and compression of symmetric bilayers. First, consider a symmetric bilayer for which both leaflets contain the same number of molecules and, in the case of a multi-component membrane, the same mole fractions of the different components.

If such a symmetric bilayer attains a tensionless state with $\Sigma = \Sigma_{\text{upp}} + \Sigma_{\text{low}} = 0$, both leaflet tensions must vanish, as well i.e.,

$$\Sigma_{\text{low}} = \Sigma_{\text{upp}} = 0 \text{ for a symmetric and tensionless bilayer.} \quad (21)$$

Likewise, the average molecular area must have the same value, $a_{\text{upp}}^0 = a_{\text{low}}^0 = a^0$, in both tensionless leaflets. Furthermore, when we examine the low-tension regime close to $\Sigma = 0$, we find a linear relationship between the bilayer tension Σ and the dimensionless area dilation Δ as given by

$$\Sigma \approx K_A \Delta \quad \text{to leading order in } \Delta \equiv \frac{a - a^0}{a^0}, \quad (22)$$

from which we obtain the area compressibility modulus K_A . Mechanical stability of the bilayer implies that the area compressibility K_A is positive. It then follows, in agreement with our intuition, that a positive bilayer tension $\Sigma > 0$ leads to an increased molecular area $a > a^0$, corresponding to a stretching of the bilayer, whereas a negative tension $\Sigma < 0$ implies a reduced molecular area $a < a^0$, corresponding to a compression of the bilayer.

Bending rigidity of lipid bilayers. In real systems, symmetric bilayers as discussed in the previous paragraph are somewhat exceptional, but they provide a useful reference system because their curvature elasticity is governed by a single elastic parameter, the bending rigidity κ , originally introduced by Canham [13] and Helfrich [14]. The value of this curvature-elastic parameter, which has the dimension of an energy, can be obtained from a systematic analysis of the membrane's shape fluctuations. For a one-component bilayer, the deduced K -value was found to satisfy the simple relationship [9,16].

$$\kappa = K_A \ell_{\text{me}}^2 / 48 \quad (23)$$

with the area compressibility modulus K_A , as defined in Eq. (22), and the bilayer thickness ℓ which is typically between 4 and 5 nm. The relationship

as given by Eq. (23) has been criticized by other groups who claimed that the prefactor $1/48$ should be replaced by $1/24$ [49,50]. However, we have recently confirmed the prefactor $1/48$ for two-component bilayers over a wide range of lipid compositions, see the fluctuation spectra in Fig. 9 [10]. The relation as given by Eq. (23) can be used to obtain a reliable estimate for the bending rigidity κ from the area compressibility modulus K_A which is computationally much less expensive than the fluctuation analysis.

Stretching and compression of asymmetric bilayers. The relation as given by Eq. (22) describes the local elastic response of a symmetric bilayer to the overall bilayer tension Σ . It is not difficult to generalize this relation to asymmetric bilayers by replacing it by two relations for the individual leaflets. Thus, we can now allow the two leaflets of the bilayer to contain different numbers of molecules as well as different mole fractions for the different components. For simplicity, we also assume that each leaflet has a uniform composition without any tendency to undergo lipid phase separation. In general, the lower and upper leaflets will then have different molecular areas, a_{low} and a_{upp} . Furthermore, the two leaflets may have different area compressibilities, K_{low} and K_{upp} , which leads to the leaflet tensions.

$$\Sigma_{\text{low}} \approx K_{\text{low}} \Delta_{\text{low}} \quad \text{for small } \Delta_{\text{low}} \equiv \frac{a_{\text{low}} - a_{\text{low}}^0}{a_{\text{low}}^0} \quad (24)$$

and

$$\Sigma_{\text{upp}} \approx K_{\text{upp}} \Delta_{\text{upp}} \quad \text{for small } \Delta_{\text{upp}} \equiv \frac{a_{\text{upp}} - a_{\text{upp}}^0}{a_{\text{upp}}^0} \quad (25)$$

where Δ_{low} and Δ_{upp} denote the area dilations of the lower and upper leaflet.

For an asymmetric and *tensionless* bilayer, the leaflet tensions satisfy $\Sigma_{\text{low}} = -\Sigma_{\text{upp}}$ as in Eq. (20). The latter condition can be fulfilled in three different ways:

- (i) First, the lower leaflet is stretched with $\Sigma_{\text{low}} > 0$ and $a_{\text{low}} > a_{\text{low}}^0$ while the upper leaflet is compressed with $\Sigma_{\text{upp}} < 0$ and $a_{\text{upp}} < a_{\text{upp}}^0$. To reduce the elastic energy stored in the two leaflets, the bilayer prefers to bulge toward the upper leaflet, thereby expanding the upper leaflet and shrinking the lower one. This situation applies to the two-component bilayer displayed in Fig. 10 with a larger mole fraction ϕ_{upp} of LH lipids in the upper leaflet;

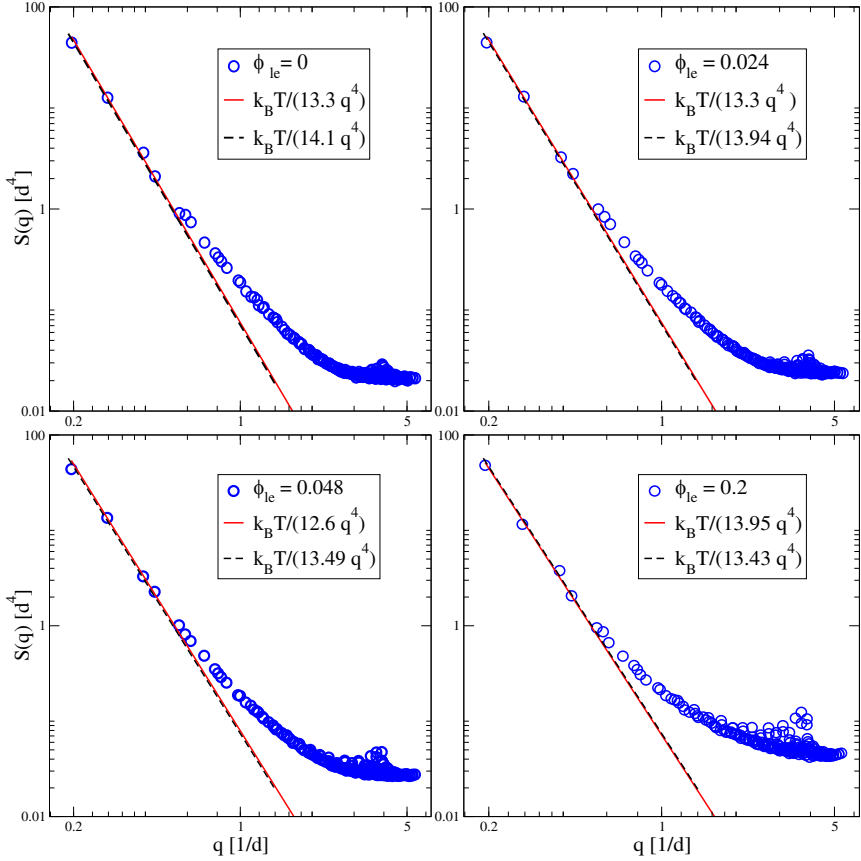


Fig. 9 Fluctuation spectra $S(q)$ of ~~and~~ tensionless bilayers with two lipid components as a function of wavenumber q . The different panels correspond to different lipid compositions as described by the mole fraction ϕ_{le} of the large-headgroup lipids. For all mole fractions, the low- q part of the spectrum behaves as $S(q) \approx k_B T / (\kappa q^4)$ with composition-dependent κ -values. The bending rigidities κ , as obtained from the spectra, the area compressibility modulus K_A , and the membrane thickness ℓ_{me} , as determined by independent analysis, are found to satisfy the relationship $\kappa = K_A \ell_{me}^2 / 48$ for all lipid compositions [10].

- (ii) Second, the lower leaflet is compressed with $\Sigma_{low} < 0$ and $a_{low} < a_{low}^0$ whereas the upper leaflet is stretched with $\Sigma_{upp} > 0$ and $a_{upp} > a_{upp}^0$. The bilayer now prefers to bulge toward the lower leaflet, thereby expanding the lower leaflet and shrinking the upper one; and
- (iii) Third, both leaflet tensions vanish, i.e., $\Sigma_{low} = \Sigma_{upp} = 0$, and both leaflets have their optimal areas per lipid, $a_{low} = a_{low}^0$ and $a_{upp} = a_{upp}^0$.

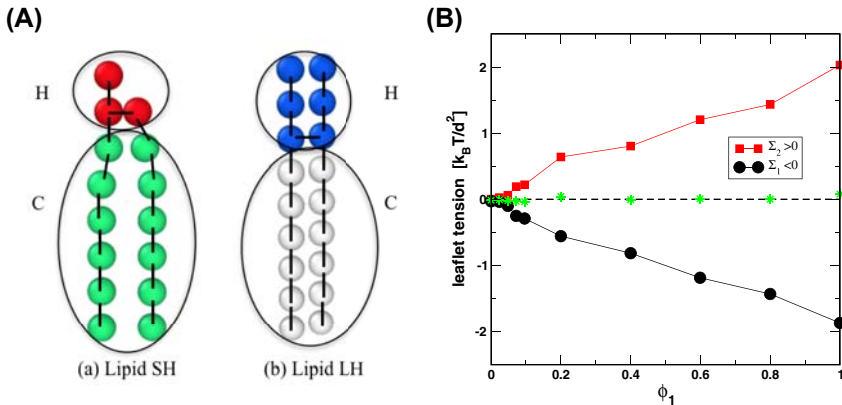


Fig. 10 Asymmetric and tensionless bilayers assembled from two lipid components, SH and LH: (A) Molecular architecture of small-head (SH) and large-head (LH) lipids. In both cases, the hydrocarbon chains are described by 2×6 chain (C) beads (green or gray). The head group of the SH lipid consists of three H beads (red), the one of the LH lipid of six H beads (blue); and (B) Upper leaflet tension $\Sigma_1 = \Sigma_{\text{upp}} < 0$ (black circles) and lower leaflet tension $\Sigma_2 = \Sigma_{\text{low}} = -\Sigma_{\text{upp}} > 0$ (red squares) as a function of mole fraction $\phi_1 = \phi_{\text{upp}}$ of the LH lipids in the upper leaflet. The lower leaflet contained no LH lipids and both leaflets were built up from the same total number of lipids. The values of the mechanical tension $\Sigma = \Sigma_{\text{upp}} + \Sigma_{\text{low}}$ are also included (green stars) and exhibit small deviations from $\Sigma = 0$ (horizontal broken line). As in Fig. 8, the midplane of the bilayer was again located at the maximum of the chain bead density. Because the upper leaflet is compressed and the lower leaflet is stretched, the bilayer prefers to bulge toward the upper leaflet [10].

In case (iii), one might expect that the bilayer has no tendency to curve toward one of the leaflets. However, a more systematic approach to determine the spontaneous curvature of a planar bilayer is provided by the first moment of the stress profile $s(z)$ as explained in the next paragraph [9,10,51–53]. The first moment of the stress profile can be finite for an asymmetric planar bilayer even if both leaflet tensions vanish as explicitly shown in a recent study of two-component bilayers containing the phospholipid POPC and the glycolipid (ganglioside) GM1 [11].

Stress asymmetry of tensionless bilayers. To examine the relation between bilayer asymmetry and spontaneous curvature in a more quantitative manner, we now consider the first moment of the stress profile $s(z)$ as given by

$$\mathcal{F} \equiv \int_{-\infty}^{+\infty} dz \mathbf{s}(z)z = \int_{-\infty}^{+\infty} dz' \mathbf{s}'(z')z' + \Sigma z_0 \quad (26)$$

where the second equality has been obtained by a change of variables from z to $z' \equiv z - z_0$, corresponding to a shift of the z -coordinate by z_0 , and $\mathbf{s}'(z') \equiv \mathbf{s}(z' + z_0)$. To ensure that the value of \mathcal{F} does not depend on the choice of the z -coordinate, we supplement the definition of \mathcal{F} in Eq. (26) by the condition that the bilayer tension Σ vanishes. We then obtain the stress asymmetry

$$\mathcal{F}^0 = \int_{-\infty}^{+\infty} dz \mathbf{s}(z)z = \int_{-\infty}^{+\infty} dz' \mathbf{s}'(z')z' \text{ for any value of } z_0 = z - z' \quad (27)$$

which we can interpret as the microscopic torque per unit length acting on a perpendicular section across the bilayer [9].

Even though the stress asymmetry \mathcal{F}^0 does not depend on the choice of the z -coordinate, it is useful to choose the origin, $z = 0$, to coincide with the midplane of the bilayer in order to obtain an intuitive interpretation of \mathcal{F}^0 [9–11]. With the midplane at $z = 0$, the upper leaflet is located at $z > 0$ while the lower leaflet is at $z < 0$. The stress asymmetry \mathcal{F}^0 can now be decomposed into two torques per unit length, $\mathcal{F}_{\text{upp}}^0$ and $\mathcal{F}_{\text{low}}^0$, arising from the upper and lower leaflet of the planar bilayer. This decomposition is provided by

$$\mathcal{F}^0 = \mathcal{F}_{\text{upp}}^0 - \mathcal{F}_{\text{low}}^0 \quad (28)$$

with

$$\mathcal{F}_{\text{upp}}^0 \equiv \int_0^{+\infty} dz \mathbf{s}(z)z \quad \text{and} \quad \mathcal{F}_{\text{low}}^0 \equiv \int_{-\infty}^0 dz \mathbf{s}(z)|z| \quad (29)$$

where the factor z has been replaced by $|z|$ in the integrand of $\mathcal{F}_{\text{low}}^0$ to compensate the minus sign in front of $\mathcal{F}_{\text{low}}^0$. For a symmetric bilayer, the stress profile $s = s_{\text{sy}}$ satisfies $s_{\text{sy}}(-z) = s_{\text{sy}}(z)$ which implies the torque balance $\mathcal{F}_{\text{upp}}^0 = \mathcal{F}_{\text{low}}^0$ and $\mathcal{F}^0 = \mathcal{F}_{\text{upp}}^0 - \mathcal{F}_{\text{low}}^0 = 0$. Starting from such a balanced situation, we can examine the consequences of different asymmetric perturbations. Assume, for instance, that the stress profile $s(z)$ increases only within the head group layer of the upper leaflet, corresponding to an increased tension of the upper leaflet-water interface. The resulting torque unbalance $\mathcal{F}_{\text{upp}}^0 > \mathcal{F}_{\text{low}}^0$ tries to tilt a perpendicular section across

the bilayer in such a way that the upper leaflet shrinks and the lower leaflet expands.

Spontaneous curvature and nanoscopic torque. On the nanoscale, the curvature elasticity of a membrane depends on two parameters, the bending rigidity κ and the spontaneous curvature m , which determine the membrane's bending energy E_{be} as in Eq. (3). This bending energy implies a *nanoscopic torque* per unit length, \mathcal{T}_{nan} , that acts along a cut across the planar bilayer. This torque has the form [51,54,55].

$$\mathcal{T}_{\text{nan}} = \left. \frac{\partial \varepsilon_{\text{be}}}{\partial C_1} \right|_{C_1=C_2=0} = \left. \frac{\partial \varepsilon_{\text{be}}}{\partial C_2} \right|_{C_1=C_2=0} = -2\kappa m. \quad (30)$$

Identifying this nanoscopic torque with the microscopic torque \mathcal{T}^0 in Eq. (27), we obtain the relation [9,51].

$$-2\kappa m = \mathcal{T}^0 = \int_{-\infty}^{+\infty} dz s(z)z \quad \text{for a tensionless bilayer.} \quad (31)$$

The same relation has also been obtained for surfactant bilayers using local density functionals and mean field theories for these bilayers [52,53].

As explained at the beginning of this paper, the spontaneous curvature m can be positive or negative and its sign requires a certain convention as explained in Fig. 3. For a planar bilayer as considered here, the spontaneous curvature is taken to be positive if the bilayer prefers to bulge toward the upper leaflet. This sign convention is in agreement with Eq. (31). Indeed, the microscopic torque $\mathcal{T}^0 = \mathcal{T}_{\text{upp}}^0 - \mathcal{T}_{\text{low}}^0$ is positive for an increased positive stress in the head group layer of the upper leaflet which implies that this torque tries to tilt a perpendicular section across the bilayer in such a way that the upper leaflet shrinks and the lower leaflet expands. As a consequence, the bilayer prefers to bulge toward the lower leaflet, corresponding to a negative spontaneous curvature, $m < 0$, in Eq. (31).

Spontaneous curvature for different bilayer asymmetries. The relationship in Eq. (31) provides an explicit connection between the stress asymmetry \mathcal{T}^0 of the molecular bilayer and the curvature-elastic parameters κ and m , i.e., between the molecular and the nanoscopic description of the bilayer membrane. This relationship has been recently used to determine the spontaneous curvature m generated by different asymmetries between the two bilayer leaflets. The presumably simplest example is provided by a bilayer that contains only a single lipid component but is assembled with different numbers of lipids, N_{upp} and N_{low} , in the upper and lower leaflet,

as in Fig. 8. The bilayer asymmetry can then be characterized by the mole fraction

$$\phi_{\text{upp}} \equiv \frac{N_{\text{upp}}}{N_{\text{upp}} + N_{\text{low}}} \quad \text{or its deviation } \phi_{\text{upp}} - 1/2 \quad (32)$$

from the symmetric case with $\phi_{\text{upp}} = 1/2$. This bilayer asymmetry in the lipid numbers is equivalent to an asymmetry in the lipid densities because both leaflets of a planar bilayer have the same area \mathcal{A} as determined by the cross section of the simulation box. Likewise, instead of the lipid density, we may also take its inverse, which represents the area per lipid, to characterize the asymmetry of the two leaflets. From the molecular simulations in Ref. [9], we obtained a linear dependence between the spontaneous curvature m and the bilayer asymmetry $\phi_{\text{upp}} - 1/2$ as given by

$$m = m_{\text{das}}(\phi_{\text{upp}} - 1/2) \quad \text{with} \quad m_{\text{das}} = \frac{4.8}{d} \simeq \frac{6}{\text{nm}} \quad (33)$$

where we used the bead diameter $d \simeq 0.8$ nm and the subscript ‘das’ stands for ‘density asymmetry’. From a physical point of view, the absolute value of the spontaneous curvature m should stay below the inverse bilayer thickness which implies that physically meaningful m -values are obtained for

$$0.47 \lesssim \phi_{\text{upp}} \lesssim 0.53 \quad \text{corresponding to} \quad -\frac{1}{6 \text{ nm}} \lesssim m \lesssim +\frac{1}{6 \text{ nm}} \quad (34)$$

as follows from Eq. (33).

Another type of bilayer asymmetry can be studied if the bilayer is assembled from two lipid components, say SH and LH as in Fig. 10A, with different compositions in the two leaflets. To distinguish this compositional asymmetry from the density asymmetry as described by $\phi - 1/2$, we assembled the bilayer with the same total lipid number, $N_{\text{upp}} = N_{\text{low}} = N_{\text{le}}$, in each leaflet but with different mole fractions

$$\phi_{\text{upp}}^{\text{LH}} \equiv \frac{N_{\text{upp}}^{\text{LH}}}{N_{\text{le}}} \quad \text{and} \quad \phi_{\text{low}}^{\text{LH}} \equiv \frac{N_{\text{low}}^{\text{LH}}}{N_{\text{le}}} \quad (35)$$

of the LH lipids in the upper and the lower leaflet. Such a compositional asymmetry also generates a spontaneous curvature that varies linearly with the mole fractions $\phi_{\text{upp}}^{\text{LH}}$ and $\phi_{\text{low}}^{\text{LH}}$. More precisely, from the simulation data, we found that the spontaneous curvature m behaves as [10]

$$m = m_{\text{cas}} \left(\phi_{\text{upp}}^{LH} - \phi_{\text{low}}^{LH} \right) \quad \text{with} \quad m_{\text{cas}} = \frac{0.32}{d} \simeq \frac{0.4}{\text{nm}} \quad (36)$$

where the subscript ‘cas’ stands for ‘compositional asymmetry’. Other types of bilayer asymmetries that have also been studied using the same computational approach, include asymmetric adsorption [9] and depletion [56] layers of small solute molecules.

In all of these simulation studies of the spontaneous curvature, the lipid molecules did not undergo flip-flops, i.e., they did not move from one leaflet to the other on the time scales of the simulations. As a consequence, each leaflet contained a constant, quenched number of lipids sustaining a constant leaflet tension for a fixed geometry of the simulation box. However, when the bilayer contains a molecular component that undergoes frequent flip-flops, the leaflet tensions change and relax toward a reference state with tensionless leaflets when the initial bilayer was tensionless [11].

From tensionless bilayers to tensionless leaflets. To elucidate this relaxation of the leaflet tensions, let us now start from a planar and tensionless bilayer with $\Sigma = 0$ which implies, in general, that the two leaflet tensions satisfy $\Sigma_{\text{low}} = -\Sigma_{\text{upp}}$ as in Eq. (20). As a consequence, one leaflet is stretched whereas the other leaflet is compressed. In such a situation, we can lower the elastic energy of the planar bilayer by reshuffling molecules from the compressed leaflet to the stretched one, thereby reducing both the positive tension in the stretched leaflet and the absolute value of the negative tension in the compressed leaflet. For a sufficiently large number of membrane molecules, we can then reach a bilayer state in which both leaflet tensions Σ_{upp} and Σ_{low} vanish.

The relaxation process just described as a steered reshuffling of molecules between the two leaflets can also occur spontaneously if a molecular component is added to the bilayer that undergoes frequent flip-flops between the two leaflets. The latter process has been recently observed by molecular dynamics simulations for a lipid bilayer that contained the phospholipid POPC and the glycolipid (ganglioside) GM1, both of which did not undergo flip-flops, and, in addition, a model cholesterol, which moved frequently from one leaflet to the other on the time scale of the simulations, as schematically shown in Fig. 11 [11].

The corresponding simulation data are displayed in Fig. 12. The upper leaflet of the asymmetric bilayer contains 66 POPCs and 24 GM1s whereas the lower leaflet is composed of 87 POPCs. In addition, the bilayer contains 20 cholesterol molecules that undergo frequent flip-flops between the two leaflets. As

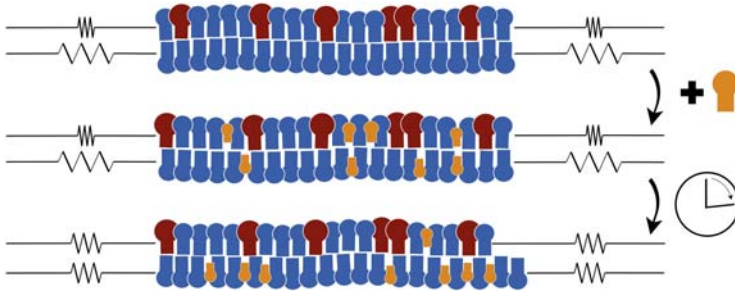


Fig. 11 Relaxation of leaflet tensions: The top row shows a bilayer membrane with two lipid components (blue and red) that do not undergo flip-flops from one leaflet to the other. The bilayer is tensionless in the sense that the bilayer tension $\Sigma = \Sigma_{\text{low}} + \Sigma_{\text{upp}}$ is (close to) zero. However, the upper leaflet of the bilayer is compressed by a negative leaflet tension $\Sigma_{\text{upp}} < 0$ whereas the lower leaflet is stretched by a positive leaflet tension $\Sigma_{\text{low}} > 0$, as indicated by the schematic springs on the left and on the right of the bilayer. As a third component, cholesterol (orange) is added to both leaflets so that they initially contain the same number of cholesterol molecules, as depicted in the middle row. After the cholesterol has been redistributed by flip-flops, both leaflets have attained a tensionless state as indicated by the relaxed springs. The cartoon at the bottom also indicates that the two tensionless leaflets typically differ in their preferred areas, which they would assume in a symmetric bilayer [11].

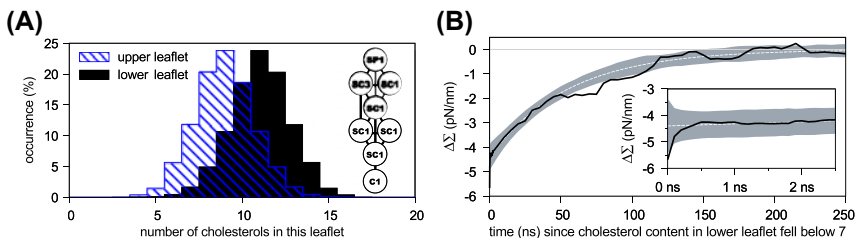


Fig. 12 Simulation data for an asymmetric bilayer with 66 POPCs and 24 GM1s in the upper leaflet, 87 POPCs in the lower leaflet, and 20 cholesterol flip-flopping between the two leaflets: (A) Different distributions for the number of cholesterol molecules in the two bilayer leaflets, with an average number of 9 cholesterol molecules in the upper leaflet (striped blue) and of 11 cholesterol in the lower leaflet (black); and (B) Time-dependent relaxation (black solid line) of $\Delta\Sigma = \Sigma_{\text{upp}} - \Sigma_{\text{low}}$ toward the state with tensionless leaflets and $\Delta\Sigma = 0$. After the first 500 ps, the relaxation curve is well fitted by a single exponential with a time constant of 55 ns. The inset displays the non-exponential behavior observed during the first 2.5 ns. [11].

shown in Fig. 12A, these cholesterol molecules are distributed in an asymmetric manner between the two leaflets, with an average number of 9 cholesterol molecules in the upper leaflet and of 11 cholesterol molecules in the lower leaflet. In this way, the flip-flopping cholesterol ensures that both leaflets are tensionless.

The time-dependent relaxation toward these tensionless leaflets is depicted in Fig. 12B. After the first 500 ps, the decay curve is well fitted by a single exponential with a time constant of 55 ns.



6. Shape transformations of nanovesicles

Lipid bilayers and biomembranes form nanovesicles with a diameter between 20 and 200 nm. Electron microscopy studies have shown that these vesicles can attain both spherical and nonspherical shapes. However, the insight obtained from electron microscopy studies of nanovesicle shapes is quite limited because the corresponding images provide only a single snapshot of each vesicle. In contrast, molecular dynamics simulations can monitor the morphologies of individual nanovesicles as we vary a certain control parameter such as the vesicle volume. Recently, we studied how nanovesicles respond to such volume changes mimicking the experimental procedure of osmotic deflation. As a result, we found that spherical nanovesicles can transform into a multitude of nonspherical shapes, see Fig. 13 [12].

Initial assembly of spherical nanovesicles. As for the planar bilayer simulations in Refs. [9,10], we used a coarse-grained molecular model for the lipid and water molecules, which are built up from beads with diameter $d \approx 0.8$ nm. We first assembled spherical vesicles by placing lipid molecules onto two spherical shells corresponding to the two leaflets of the bilayer membranes. The size of these vesicles was primarily determined by the vesicle volume, i.e., by the number of water beads enclosed by the inner leaflet of the membrane. This number was chosen in such a way that the head group layers of the inner and outer leaflets had a diameter of about $45 d$ and $50 d$, respectively. For a given volume, we placed N_{il} and N_{ol} lipids onto the inner and outer leaflets, respectively, and considered different vesicles with the same total lipid number

$$N_{lip} = N_{il} + N_{ol} = 10\,100. \quad (37)$$

Thus, for fixed volume and constant total lipid number, we are left with a single assembly parameter, which we can take to be the lipid number N_{ol} in the outer leaflet. The spherical vesicles assembled in this manner were found to be stable for a range of N_{ol} -values including the interval $5700 \leq N_{ol} \leq 6300$, corresponding to the spherical vesicles displayed in Fig. 13.

Vesicle volume and volume parameter. Experimentally, the volume of a vesicle can be changed by osmotic deflation and inflation. In the

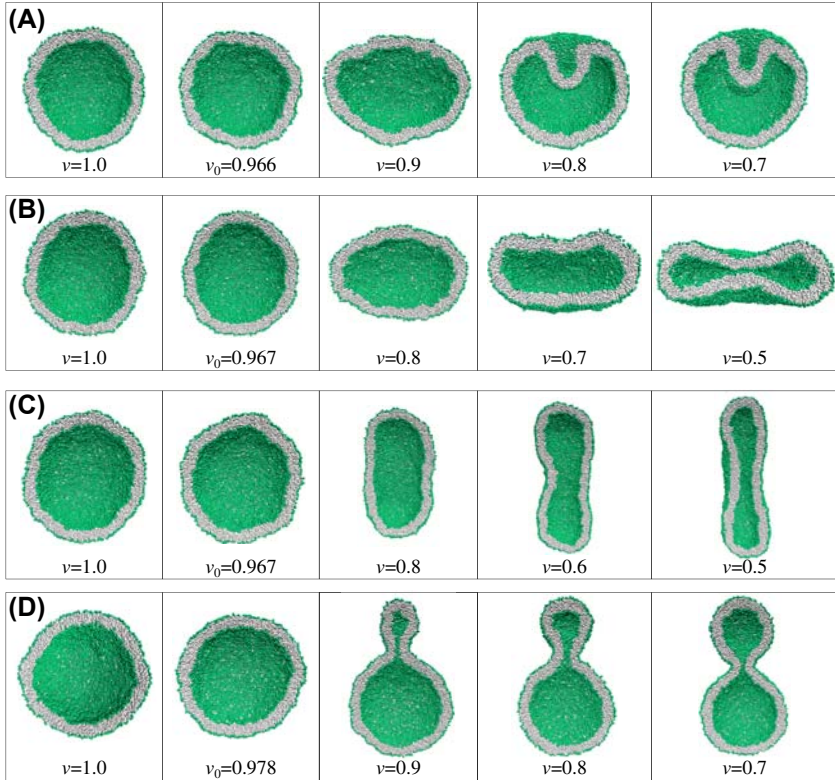


Fig. 13 Distinct shape transformations of spherical nanovesicles in response to volume reduction: Each panel (A–D) displays a series of shapes that an individual vesicle attains when we decrease its volume v as defined in Eq. (38). In all four cases, we start with a spherical vesicle (leftmost snapshots, $v = 1$) that encloses the same volume of water. In addition, all four spherical vesicles are bounded by a lipid bilayer that is built up from the same total number of lipids, N_{lip} , but differs in the lipid numbers, N_{il} and N_{ol} , that are assembled in the inner and outer leaflets of the vesicles. We first reduced the vesicle volume by a few percent to $v = v_0 < 1$ to decrease the bilayer tension by two orders of magnitude, thereby obtaining an essentially tensionless bilayer. Further volume reduction then leads to very different shapes as shown in the rightmost snapshots: (A) For $N_{il} = 4400$ in the inner leaflet and $N_{ol} = 5700$ in the outer leaflet, the vesicle transforms into a stomatocyte for $v \leq 0.8$; (B) For $N_{il} = 4200$ and $N_{ol} = 5900$, it becomes an oblate or discocyte for $v \leq 0.8$; (C) For $N_{il} = 4000$ and $N_{ol} = 6100$, it transforms into a prolate for $v \leq 0.8$; and (D) For $N_{il} = 3800$ and $N_{ol} = 6300$, it attains the shape of a dumbbell with a closed membrane neck. Thus, redistributing only 200 lipids, i.e., less than 2% of the total lipid number N_{lip} , from the inner to the outer leaflet or vice versa leads to completely different shape transformation [12].

simulations, we varied the vesicle volume by changing the number N_W of water beads enclosed by the inner leaflet of the vesicle membrane. To monitor the volume changes, we used the volume parameter ν defined by

$$\nu \equiv \frac{N_W}{N_W^{\text{isp}}} \quad (38)$$

where N_W^{isp} is the number of water beads enclosed by the initial spherical vesicle. Thus, the initial vesicle is characterized by $\nu = 1$ and any volume reduction with $N_W < N_W^{\text{isp}}$ leads to $\nu < 1$. Monitoring volume changes via the parameter ν is rather convenient in the simulations because we can directly change the number N_W of water beads within the vesicle and thus compute the value of ν without the necessity to determine any membrane surface, see Fig. 13. Therefore, the volume parameter ν as defined by Eq. (38) is not quite identical with the volume-to-area ratio ν as defined by Eq. (6) in the context of curvature models but both ν and ν vanish for vanishing volume and increase monotonically with increasing volume. One difference between the two parameters is that the volume-to-area ratio ν cannot exceed the value $\nu = 1$, corresponding to a sphere, whereas the initially assembled sphere with $\nu = 1$ can be further inflated by adding water to it, which leads to $\nu > 1$.

Stretching and compression of bilayer leaflets. The distinct shape transformations of spherical nanovesicles as illustrated in Fig. 13 can be understood by examining how the different lipid numbers N_{il} and N_{ol} change the areas per lipid in the two leaflets of the bilayers. Indeed, when we place, for fixed vesicle volume, somewhat different numbers of lipids on the inner and outer leaflets of the spherical bilayers, we obtain different molecular areas, a_{il} and a_{ol} , for the lipids in the two bilayer leaflets. In all cases, the lipid area a_{il} within the inner leaflet is larger than the lipid area a_{ol} within the outer leaflet which implies that the outer leaflets are more densely packed [12].

Intuitively, we expect that the inner and the outer leaflet of the vesicle membrane have an optimal area per lipid, a_{il}^0 and a_{ol}^0 , corresponding to their natural packing densities and their elastically relaxed states. Let us assume, for a moment, that we knew these optimal lipid areas. If we now stretched the outer leaflet of the spherical bilayer, we would increase the lipid area to $a_{\text{ol}} > a_{\text{ol}}^0$. On the other hand, if we compressed the outer leaflet, we would reduce this lipid area to $a_{\text{ol}} < a_{\text{ol}}^0$. The same behavior applies to the inner leaflet of the spherical bilayer: $a_{\text{il}} < a_{\text{il}}^0$ will be caused by compression and $a_{\text{il}} > a_{\text{il}}^0$ by stretching of the inner leaflet.

To determine the optimal lipid areas a_{il}^0 and a_{ol}^0 , we need to know the mechanical tensions, Σ_{il} and Σ_{ol} , that act within the inner and outer leaflets. As for a planar bilayer, see Fig. 8, these tensions can be obtained by a two-step procedure. First, we calculate the stress profile across the spherical bilayer. Subsequently, we define the location of the midsurface to identify the spatial regions that are occupied by the two leaflets and to decompose the overall bilayer tension into two separate contributions.

Stress profile and bilayer tension of spherical bilayer. Because of the spherical symmetry, the local stress or pressure tensor has the general form [12].

$$\mathbf{P} = P_{\text{N}}(r)\mathbf{e}_r \otimes \mathbf{e}_r + P_{\text{T}}(r)[\mathbf{e}_\theta \otimes \mathbf{e}_\theta + \mathbf{e}_\phi \otimes \mathbf{e}_\phi] \quad (39)$$

with the normal component $P_{\text{N}}(r)$ and the tangential component $P_{\text{T}}(r)$ where \mathbf{e}_r , \mathbf{e}_θ , and \mathbf{e}_ϕ are orthogonal unit vectors and the symbol \otimes represents the dyadic product. The numerical values of $P_{\text{N}}(r)$ and $P_{\text{T}}(r)$ as well as the stress profile $s(r) \equiv P_{\text{N}}(r) - P_{\text{T}}(r)$ can be calculated using the computational method described in Refs. [57,58]. We found that the stress profile $s(r)$ changes strongly when we reshuffle lipids from one leaflet to the other, thereby changing the lipid numbers N_{ol} and $N_{\text{il}} = N_{\text{lip}} - N_{\text{ol}}$. The bilayer tension Σ can then be obtained by the integral [12]

$$\Sigma = \int_0^\infty dr [P_{\text{N}}(r) - P_{\text{T}}(r)] = \int_0^\infty dr s(r), \quad (40)$$

in close analogy to the interfacial tension [45] of a spherical liquid droplet.

Midsurface and leaflet tensions of spherical bilayer. As for a planar bilayer, we have several options to define the midsurface of a spherical bilayer. The simplest option is to locate the midsurface at the peak of the density profile $\rho_{\text{C}}(r)$ for the hydrocarbon chains which are represented here by chain (C) beads, see Fig. 7 for the corresponding density profile across the planar bilayer. The corresponding midsurface radius $R_{\text{mid}} = R_{\text{C}}$ was found to be $R_{\text{C}} = (22.05 \pm 0.05) d$ for all four spherical vesicles in Fig. 11.

After having determined the midsurface radius R_{C} , we compute the leaflet tensions Σ and Σ_{ol} via the integrals

$$\Sigma_{\text{il}} = \int_0^{R_{\text{C}}} dr s(r) \quad \text{and} \quad \Sigma_{\text{ol}} = \int_{R_{\text{C}}}^\infty dr s(r). \quad (41)$$

Note that a negative leaflet tension implies a compressed leaflet whereas a positive leaflet tension corresponds to a stretched leaflet. The numerical values of the leaflet tensions Σ_{il} and Σ_{ol} as obtained from Eq. (41) for the four spherical vesicles in Fig. 1 with $\nu = 1$ are plotted in Fig. 14. Interpolation of these two sets of data leads to two straight lines which cross at $N_{ol}^* = 5963$, corresponding to equal leaflet tensions $\Sigma_{il} = \Sigma_{ol} \approx 0.18k_B T/d^2$.

Spherical vesicle with tensionless leaflets. We then studied a spherical vesicle with $N_{ol} = N_{ol}^*$ and $N_{il} = N_{il}^* = N_{lip} - N_{ol}^*$, see Fig. 15, that encloses the same number of water beads, $N_W^{isp} = 90\,400$, as the four spherical vesicles in Fig. 13. When we slightly deflated this vesicle and reduced its volume to $N_W = 87360$, we obtained another spherical vesicle for which both leaflet tensions $\Sigma_{ol} \approx 0$ and $\Sigma_{il} \approx 0$, i.e., for which both leaflet tensions vanished individually. This reference state with tensionless leaflets has the reduced volume $\nu = \nu_0 = 0.966$ as well as the lipid areas, $a_{ol}^0 = 1.139d^2$ and $a_{il}^0 = 1.318d^2$, corresponding to a more loosely packed inner leaflet and a more closely packed outer one. As shown in Fig. 15, a further reduction of the volume leads to prolates and discocytes.

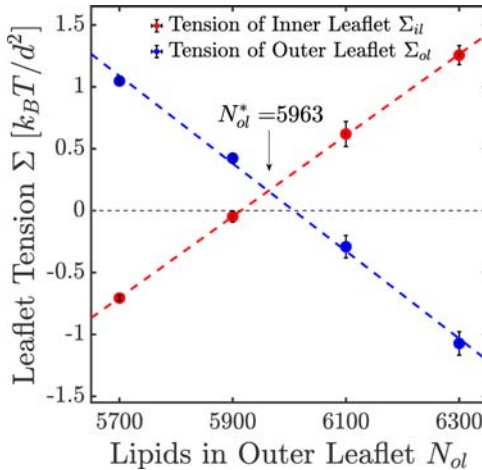


Fig. 14 Leaflet tensions Σ_{il} (red) and Σ_{ol} (blue) of the inner and outer bilayer leaflets as functions of the lipid number N_{ol} in the outer leaflet for the four spherical vesicles displayed in Fig. 1 with fixed total number $N = N_{il} + N_{ol} = 10\,100$ and volume parameter $\nu = 1$. The tension Σ_{il} in the inner leaflet increases whereas the tension Σ_{ol} in the outer leaflet decreases with increasing N_{ol} . Furthermore, both sets of data are well fitted by straight lines which cross at $N_{ol}^* = 5963$, corresponding to equal leaflet tensions $\Sigma_{il} = \Sigma_{ol} \approx 0.18k_B T/d^2$ [12].

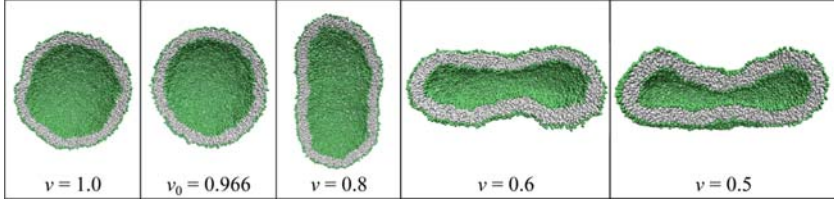


Fig. 15 Shape transformations of the spherical nanovesicle with tensionless leaflets, assembled from $N_{ol}^* = 5963$ and $N_{il} = 4137$ lipids in the outer and inner leaflet, respectively. For the initial vesicle with volume parameter $\nu = 1$, the two leaflet tensions Σ_{il} and Σ_{ol} have the same values as determined in Fig. 14. For the spherical vesicle with volume parameter $\nu = \nu_0 = 0.966$ both leaflet tensions vanish providing the unique reference state for the chosen total number of lipids, $N_{lip} = 10\,100$. As we continue to reduce the vesicle volume, the vesicle attains a prolate shape for $\nu = 0.8$ and $\nu = 0.7$, an oblate or discocyte shape for $\nu = 0.6$, and a stomatocyte shape for $\nu = 0.5$ [12].

For planar membranes, the reference state of a one-component bilayer with $\Sigma_{low} = \Sigma_{upp} = 0$ is provided by a symmetric and tensionless bilayer [9]. In this case, both leaflets contain the same number of lipids, $N_{upp} = N_{low}$ and have the same area per lipid, $a_{upp}^0 = a_{low}^0$. In contrast, for the spherical nanovesicles considered here, the reference state with tensionless leaflets $\Sigma_{il} = \Sigma_{ol} = 0$ is characterized by $N_{il} < N_{ol}$ and $a_{il} > a_{ol}$.

Spontaneous curvature of spherical bilayer. For a planar and tensionless bilayer, the first moment of the stress profile $s(z)$ can be interpreted as the stress asymmetry or microscopic torque \mathcal{F}^0 acting on a perpendicular section across the bilayer per unit length. The nanoscopic torque of a planar curvature-elastic membrane, on the other hand, is equal to $-2\kappa m$. Identifying the microscopic with the nanoscopic torque leads to Eq. (31), which allows us to calculate the spontaneous curvature from the stress profile [9,51]. Extending the latter approach to a spherical bilayer and using the expression [54,55]

$$\mathcal{F}_{nan} = 2\kappa(M_{sp} - m) \quad (42)$$

for the nanoscopic torque of a spherical curvature-elastic membrane with mean curvature M_{sp} , we obtain the relation [12].

$$2\kappa(M_{sp} - m) = \mathcal{F}^0 = \int_0^\infty dr s(r)r(\text{bilayer tension } \Sigma = 0) \quad (43)$$

between the bending rigidity κ , the mean curvature M_{sp} of the spherical vesicle, the spontaneous curvature m , and the stress asymmetry or first

moment \mathcal{T}^0 of the stress profile $s(r)$ where the superscript 0 reminds us that the spherical bilayer is again tensionless.

We can now apply the relation in Eq. (43) to the five spherical vesicles in Figs. 13 and 15 with volume parameter $\nu = \nu_0 < 1$, corresponding to tensionless bilayers with $\Sigma = \Sigma_{\text{ol}} + \Sigma_{\text{il}} = 0$. It is also convenient to replace the outer leaflet number N_{ol} , which is of the order of 10^4 , by the corresponding mole fraction

$$\varphi_{\text{ol}} \equiv \frac{N_{\text{ol}}}{N_{\text{ol}} + N_{\text{il}}}, \quad (44)$$

which is of the order of one, in close analogy to the lipid mole fraction φ_{upp} for the upper leaflet of the planar bilayer in Eq. (32). All five vesicles have essentially the same radius $R_{\text{sp}} = 1/(22d)$ and, thus, the same mean curvature, $M_{\text{sp}} = 1/R_{\text{sp}}$, and their membranes have roughly the same bending energy $\kappa \approx 15 k_B T$. A computation of the stress asymmetry \mathcal{T}^0 then leads to the spontaneous curvature [12]

$$m = m_{\text{das}}(\varphi_{\text{ol}} - 0.587) \quad \text{with} \quad m_{\text{das}} = \frac{5.05}{d} \approx \frac{6.3}{\text{nm}} \quad (45)$$

which applies to

$$5700 \leq N_{\text{ol}} \leq 6300 \quad \text{or} \quad 0.564 \leq \varphi_{\text{ol}} \leq 0.624. \quad (46)$$

Thus, the spontaneous curvature m for a spherical vesicle with radius $R_{\text{sp}} = 22d$ vanishes for $\varphi_{\text{ol}}^{\text{sy}} = 0.587$ or $N_{\text{ol}} = 5929$. Comparison with the corresponding Eq. (33) for the planar bilayer shows that the mole fraction $\varphi_{\text{upp}}^{\text{sy}} = 1/2$ for a symmetric planar bilayer has now been shifted to the mole fraction $\varphi_{\text{ol}}^{\text{sy}} = 0.587$ for a symmetric spherical bilayer. Likewise, the curvature scale $m_{\text{das}} = 4.8/d$ for the planar bilayer has been increased to $m_{\text{das}} = 5.05/d$ for the spherical bilayer. Both $\varphi_{\text{ol}}^{\text{sy}}$ and m_{das} are expected to depend on the sphere radius R_{sp} of the spherical vesicle and should approach the values for the planar bilayer in the limit of large R_{sp} .



7. Two-sphere vesicles and membrane necks

In Fig. 13D, the spherical nanovesicle is transformed into a dumbbell shape consisting of two roughly spherical segments that are connected by a closed membrane neck. Such dumbbell shapes with closed necks are also observed for giant vesicles, i.e., on the scale of many micrometers, see Fig. 1A. In this section, we will show that these two-sphere morphologies

can be directly understood in the framework of curvature elasticity and that these shapes are stable within a large subregion of the morphology diagram.

Coexistence of two spherical segments. Let us again consider a large vesicle membrane with uniform curvature-elastic properties, i.e., with uniform bending rigidity κ and uniform spontaneous curvature m . The membrane experiences the pressure difference $\Delta P = P_{\text{in}} - P_{\text{ex}}$ between the interior and exterior solution as well as the mechanical tension Σ . If some membrane segment forms a spherical cap with mean curvature M_{sp} , this curvature satisfies the Euler-Lagrange or shape equation

$$\Delta P = 2\widehat{\Sigma}M_{\text{sp}} - 4\kappa mM_{\text{sp}}^2 \quad (47)$$

with the total membrane tension

$$\widehat{\Sigma} \equiv \Sigma + 2\kappa m^2 = \Sigma + \sigma$$

as defined previously in Eqs. (10) and (11). The shape Eq. (47) is quadratic in M_{sp} and can thus have two, one, or no real-valued solutions.

We now focus on two-sphere shapes as in Figs. 1A and 13D, for which both spherical segments have a positive mean curvature, and take the spontaneous curvature m to be positive as well. We then find that the quadratic shape equation has two solutions corresponding to a large and a small sphere radius,

$$R_{\text{sp}} = R_l \text{ and } R_{\text{sp}} = R_s < R_l, \text{ for } \Delta P < \frac{\widehat{\Sigma}^2}{4\kappa m}, \quad (48)$$

where the subscripts l and s stand for ‘large’ and ‘small’. The two solutions merge into a single, degenerate solution with

$$R_l = R_s = R_* \text{ for } \Delta P = \frac{\widehat{\Sigma}^2}{4\kappa m}, \quad (49)$$

corresponding to two equally sized spheres with radius R_* .

Spherical segments connected by membrane necks. So far, we paid no attention to the boundaries of the spherical segments. Inspection of the two examples in Figs. 1A and 13D reveals that the two spherical segments are in fact punctured spheres connected by closed, hourglass-shape membrane necks or ‘wormholes’. The neck shape can be explicitly resolved for the nanovesicle in Fig. 13D. Analogous necks are also formed by cellular membranes, e.g., during endo- or exocytosis and during cell division [35].

Closed necks formed by uniform membranes as considered here are governed by a relatively simple stability condition that can be expressed in terms of the spontaneous curvature m and the (effective) curvature M_{ne} of the membrane neck which is defined by Ref. [4].

$$M_{\text{ne}} \equiv \frac{1}{2}(M_l + M_s) \quad (50)$$

In Fig. 11D and Fig. 1A, both spheres of the two-sphere shapes have positive mean curvatures $M_l = 1/R_l > 0$ and $M_s = 1/R_s > 0$. In such a situation, the neck curvature $M_{\text{ne}} > 0$ and the closed membrane neck is stable if [4,20,59].

$$m \geq M_{\text{ne}} = \frac{1}{2} \left(\frac{1}{R_l} + \frac{1}{R_s} \right) > 0. \quad (51)$$

For the special case in which both spheres have the same radius R_* , corresponding to the degenerate solution in Eq. (49), the neck curvature becomes $M_{\text{ne}} = 1/R_*$ and the closed neck is stable if

$$m \geq \frac{1}{R_*} > 0 \quad (R_s = R_l = R_*). \quad (52)$$

These stability conditions for membrane necks are quite remarkable because they provide simple relations between the geometry of the two-sphere shape and the spontaneous curvature m , which represents a curvature-elastic parameter. For GUVs, the neck curvature M_{ne} can be directly determined from the optical micrographs which provides a lower bound on the spontaneous curvature m . The inequality as given by Eq. (51) directly implies that two-sphere shapes as in Fig. 1A with $M_l > 0$ and $M_s > 0$ can only form for positive spontaneous curvature. It is also important to note that the stability relation for the closed membrane neck as given by Eq. (51) is local and does not depend on any global properties of the membrane shape. As a consequence, this stability relation also applies to more complex multispheres with an arbitrary number N_l of large spheres and an arbitrary number N_s of small spheres as discussed in the next section.

Tension and pressure for two-sphere shapes. The two solutions R_l^{-1} and R_s^{-1} of the spherical shape equation can be used to obtain explicit expressions for the mechanical tension and the pressure difference in terms of the two radii [4]. As a result, one obtains the mechanical tension

$$\Sigma = 2\kappa m \left(\frac{1}{R_l} + \frac{1}{R_s} \right) - 2\kappa m^2 = 2\kappa m(2M_{ne} - m) \quad (53)$$

and the pressure difference

$$\Delta P = \frac{4\kappa m}{R_l R_s}. \quad (54)$$

These two relationships allow us to calculate Σ and ΔP from the experimentally observed curvature radii R_l and R_s provided we know the bending rigidity κ and the spontaneous curvature m of the vesicle membrane.

As an example, consider the symmetric dumbbell or two-sphere vesicle displayed in Fig. 1A, which consists of two equally sized spheres with radius $R_l = R_s = R_* = 3.25\mu\text{m}$. For this vesicle, the bending rigidity and the spontaneous curvature were measured to be $\kappa = 48 k_B T$ and $m = 1.45 \mu\text{m}^{-1}$ (corresponding to a solution concentration $X = 7.8 \text{ nM}$ of the His-tagged proteins and 0.1 mol% anchor lipids) [5]. Using these parameter values in Eqs. (53) and (54), we obtain the negative mechanical tension $\Sigma = -0.48 \times 10^{-6} \text{ N/m}$ and the positive pressure difference $\Delta P = 0.13 \text{ N/m}^2$. Note that the mechanical membrane tension Σ , obtained here for the symmetric dumbbell in Fig. 1A, is of the order of 10^{-6} N/m , which is indeed rather small compared to a typical interfacial tension between two liquids, which is usually of the order of 10^{-2} N/m .

Geometry of two-sphere shapes with out-buds. When we ignore the contributions of the membrane necks to the membrane area A and the vesicle volume V , we obtain the relations

$$A = 4\pi(R_l^2 + R_s^2) \quad \text{and} \quad V = \frac{4\pi}{3}(R_l^3 + R_s^3) \quad (55)$$

for the area and volume in terms of the large and small sphere radii R_l and R_s . It is now convenient to use the vesicle size

$$R_{ve} = \sqrt{A/(4\pi)} \quad (56)$$

again as the basic length scale and to introduce the dimensionless radii

$$r_l \equiv \frac{R_l}{R_{ve}} \quad \text{and} \quad r_s \equiv \frac{R_s}{R_{ve}}. \quad (57)$$

When expressed in terms of these radii, the area and volume relations in Eq. (55) attain the dimensionless form

$$1 = r_l^2 + r_s^2 \quad \text{and} \quad v = r_l^3 + r_s^3 \quad (58)$$

with the dimensionless volume-to-area ratio

$$v = \frac{V}{\frac{4\pi}{3}R_{ve}^3} = \frac{6\sqrt{\pi}V}{A^{3/2}}$$

as defined previously in Eq. (6). The two polynomial equations in Eq. (58) imply that the two-sphere shapes depend only on the volume-to-area ratio v but not on any other parameter.

Neck closure condition and limit shapes. The stability condition for the closed membrane neck as given by Eq. (51) includes the neck closure condition

$$m = M_{ne} = \frac{1}{2} \left(\frac{1}{R_l} + \frac{1}{R_s} \right) \quad (59)$$

as a limiting case. Using the dimensionless curvatures $\bar{m} = mR_{ve}$ and $\bar{M}_{ne} = M_{ne}R_{ve}$, the neck closure condition becomes

$$\bar{m} = \bar{M}_{ne} = \frac{1}{2} \left(\frac{1}{\eta} + \frac{1}{r_s} \right). \quad (60)$$

Combining this neck closure condition with the geometric relations as given by Eq. (58), we can eliminate the two radii η and r_s to obtain the functional relationship [20].

$$v = v_{1+1}(\bar{m}) = -\frac{1}{4\bar{m}^3} + \left(1 - \frac{1}{2\bar{m}^2} \right) \sqrt{1 + \frac{1}{4\bar{m}^2}} \quad \text{for } \bar{m} > \sqrt{2}. \quad (61)$$

The function $v = v_{1+1}(\bar{m})$ is plotted in the morphology diagram of Fig. 16 and describes the line of limit shapes L_{1+1} . The subscript 1 + 1 indicates a multisphere consisting of one large and one small sphere. The line of limit shapes L_{1+1} extends down to $\bar{m} = \bar{m}_* = \sqrt{2}$. At this endpoint, the limit shape L_{1+1} consists of two equally sized spheres with volume

$$v = v_{1+1}(\bar{m} = \sqrt{2}) = \frac{1}{\sqrt{2}} \equiv v_* \quad (62)$$

and with the radii

$$r_l = r_s = r_* = \frac{1}{\sqrt{2}}. \quad (63)$$

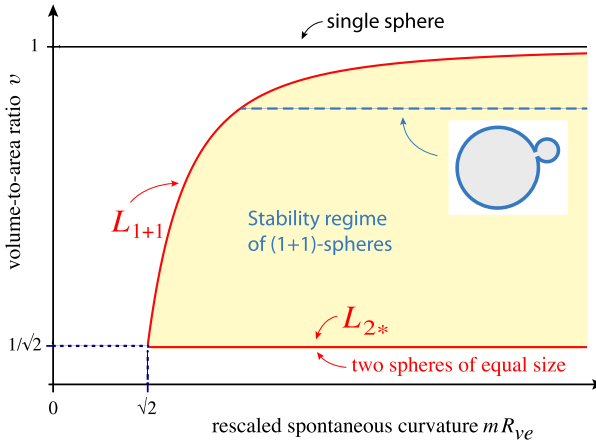


Fig. 16 Morphology diagram for positive spontaneous curvature $\bar{m} = mR_{ve} \geq 0$ and volume-to-area ratio v with $0 \leq v \leq 1$. The yellow subregion represents the stability regime for two-sphere shapes consisting of a large and a small (punctured) sphere connected by a closed membrane neck. This stability regime is located between two lines of limit shapes denoted by L_{1+1} and L_{2*} . Within the stability regime, the shapes depend only on v and not on m . Therefore, along the whole line L_{2*} , the vesicle forms always the same (1 + 1)-sphere morphology consisting of two equally sized spheres. Likewise, along the dashed horizontal line (blue), all vesicles have the shape displayed in the inset.

The endpoint with $(\bar{m}, v) = \left(\sqrt{2}, \frac{1}{\sqrt{2}}\right)$ is, in fact, a cornerpoint in the morphology diagram because it is connected to another line denoted by L_{2*} in Fig. 16. The latter line is located at

$$v = v_* = \frac{1}{\sqrt{2}} \quad \text{and} \quad \bar{m} > \sqrt{2} \quad (\text{limit shape } L_{2*}). \quad (64)$$

For all points along this line, the limit shape L_{2*} consists of two equally sized spheres.

Therefore, we conclude that the stability regime for two-sphere shapes with a closed membrane neck is located in between two lines of limit shapes, L_{1+1} and L_{2*} , as depicted by the yellow region in Fig. 16. When we start from a point (\bar{m}, v) within this stability regime and increase the spontaneous curvature m for fixed volume v , the two-sphere shape remains unchanged. Likewise, the two-sphere shape remains unchanged when we decrease the spontaneous curvature m for fixed v until we reach the limit shape L_{1+1} with $\bar{m} = \bar{m}(v)$. For the latter shape the closed neck is marginally stable and opens up when we continue to decrease m . On the other hand,

when we increase ν for fixed m , we increase the large sphere radius r_l and decrease the small sphere radius r_s , until we reach the limit shape L_{1+1} with volume $\nu = \nu_{1+1}(\bar{m})$. For the latter limit shape, the closed neck is again marginally stable and opens up when we continue to increase the volume ν . Finally, when we decrease the volume ν for fixed spontaneous curvature, we increase the small sphere radius r_s and decrease the large sphere radius r_l until we reach the limit shape L_{2*} consisting of two equally sized spheres with volume $\nu_* = 1/\sqrt{2}$. This latter shape is reached for all spontaneous curvatures $\bar{m} \geq \sqrt{2}$ because the geometry of the two-sphere vesicles is solely determined by the dimensionless volume-to-area ratio $\nu = \nu_*$.

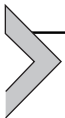
Finally, it is interesting to note the mechanical tension Σ as given by Eq. (53) has the form [43].

$$\Sigma = 2\kappa m^2 = \sigma \quad \text{for the limit shapes } L_{1+1} \quad (65)$$

and

$$\Sigma = 2\kappa m(2\sqrt{2} - m) < \sigma \quad \text{for the limit shapes } L_{2*}. \quad (66)$$

Furthermore, the mechanical tension vanishes for $m = 2M_{\text{ne}}$, which defines another line within the yellow stability regime in Fig. 16, and becomes negative when we move beyond this line to higher values of the spontaneous curvature.



8. Curvature-induced division of giant vesicles

As emphasized in the previous section, the two-sphere shapes do not depend on the spontaneous curvature m but only on the volume parameter ν . As a consequence, when we move across the yellow stability regime in Fig. 16, keeping ν fixed, we will always see the same two-sphere shape. However, the concomitant change in spontaneous curvature will change the bending energy and, more importantly, the constriction force f acting at the membrane neck.

Curvature-induced constriction force. To derive the constriction force generated by the spontaneous curvature around a closed membrane neck, we consider a convenient parametrization of a dumbbell shape, consisting of two hemispheres connected by two unduloid segments that form a narrow neck of neck radius R_{ne} [4,59]. The dumbbell with a closed neck is obtained in the limit of zero R_{ne} . To reveal the curvature-induced constriction force f , we first consider an external constriction force f_{ex} compressing

the neck. In such a situation, the bending energy E_{be} of the dumbbell has the form [4].

$$E_b(R_{ne}) \approx E_{be}(0) + f_{ex}R_{ne} + 8\pi\kappa(m - M_{ne})R_{ne} \quad (67)$$

up to first order in R_{ne} . The closed neck is stable if the term proportional to the neck radius R_{ne} increases with increasing R_{ne} which implies

$$f_{ex} + 8\pi\kappa(m - M_{ne}) > 0 \quad (\text{stably closed neck}). \quad (68)$$

In the absence of an external force, i.e., for $f_{ex} = 0$, we then obtain the curvature-induced constriction force [4].

$$f = 8\pi\kappa(m - M_{ne}) \quad (69)$$

which is proportional to the difference $m - M_{ne}$ between the spontaneous curvature m and the neck curvature M_{ne} , defined in Eq. (51), as well as to the bending rigidity κ .

The curvature difference $m - M_{ne}$ vanishes along the line L_{1+1} of limit shapes. Once we have crossed the line L_{1+1} toward higher values of the shape parameter $\bar{m} = mR_{ve}$, the curvature difference $m - M_{ne}$ increases monotonically as we increase the spontaneous curvature m for fixed volume-to-area ratio v . When the constriction force f has reached a sufficiently large value, the membrane neck should undergo fission and the GUV should be divided into two daughter vesicles.

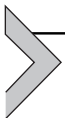
Transition state and free energy barrier for neck fission. The process of neck fission and vesicle division represents a topological transformation from the one-vesicle state provided by the dumbbell shape to the two-vesicle state of two separate daughter vesicles. Both states have essentially the same bending energy because the closed neck of the dumbbell does not contribute to this energy. However, the two states have different topologies which implies that the Gaussian curvature term in Eq. (2) makes a different contribution to the one-vesicle and to the two-vesicle state. The latter contribution is equal to $4\pi\kappa_G$ for the one-vesicle state and to $8\pi\kappa_G$ for the two-vesicle state, where κ_G is the Gaussian curvature modulus. Therefore, the difference in free energy, $G_2 - G_1$, between the two- and the one-vesicle state is equal to $4\pi\kappa_G$. Both experimental studies [60,61] and computer simulations [62] indicate that the Gaussian curvature modulus is negative with $\kappa_G \approx -\kappa$. For the lipid membranes studied here, we then obtain the estimate $\kappa_G \approx -48k_B T$ which leads to the free energy difference $G_2 - G_1 \approx -603k_B T$. Therefore, neck fission and GUV division is a strongly exergonic process and can, in principle, occur spontaneously.

However, the rate with which this process proceeds is governed by the free energy barrier that separates the one-vesicle from the two-vesicle state.

In order to cleave the neck, we have to create two bilayer pores with a diameter that is comparable to the size of the closed membrane neck before fission. The resulting free energy barrier is governed by the edges of these two pores and the associated edge energy, which is equal to the edge tension λ times the combined circumference of the two pores. To lower the barrier by a significant amount, the constriction force generated by the spontaneous curvature must perform mechanical work that is comparable to this edge energy [4]. One then finds that the neck undergoes fission if the spontaneous curvature exceeds the threshold value $m_* \equiv \lambda/(2\kappa)$.

Controlled GUV division by membrane-bound GFP. As explained in the section on fine-tuning of spontaneous curvature, membrane-bound GFP generates a significant spontaneous curvature as described by Eq. (9). When we use these spontaneous curvature values together with the bending rigidity $\kappa \simeq 48 k_B T$ in Eq. (69), we find that the membrane-bound GFP generates constriction forces up to 80 pN, comparable to the largest constriction forces generated by specialized protein complexes that cleave the necks of cellular membranes. Indeed, we have recently shown experimentally that the cleavage of membrane necks and the concomitant division of GUVs can be induced simply by an increase in the GFP solution concentration and the resulting spontaneous curvature [5]. Two examples for such a division process are shown in the panels A and B of Fig. 17.

The controlled division process consists of three steps. First, we adjust the volume of the GUV by osmotic deflation or inflation to attain an appropriate value for the volume-to-area ratio ν which is $\nu = 0.93$ in Fig. 17A and $\nu = 0.7$ in Fig. 17B. Second, we increase the GFP concentration X until the GUV attains a dumbbell shape with a closed membrane neck. Third, increasing the GFP concentration X even further leads to the cleavage of the neck and to the division of the GUV.



9. Multispherical shapes of vesicles

The two-sphere or $(1 + 1)$ -sphere shapes discussed previously, see the corresponding stability regime in Fig. 16, represents the simplest example for a stable multispherical shape. Indeed, the theory of curvature elasticity predicts stable multisphere shapes consisting of an arbitrary number of (punctured) spheres connected by closed membrane necks [4,35]. This follows

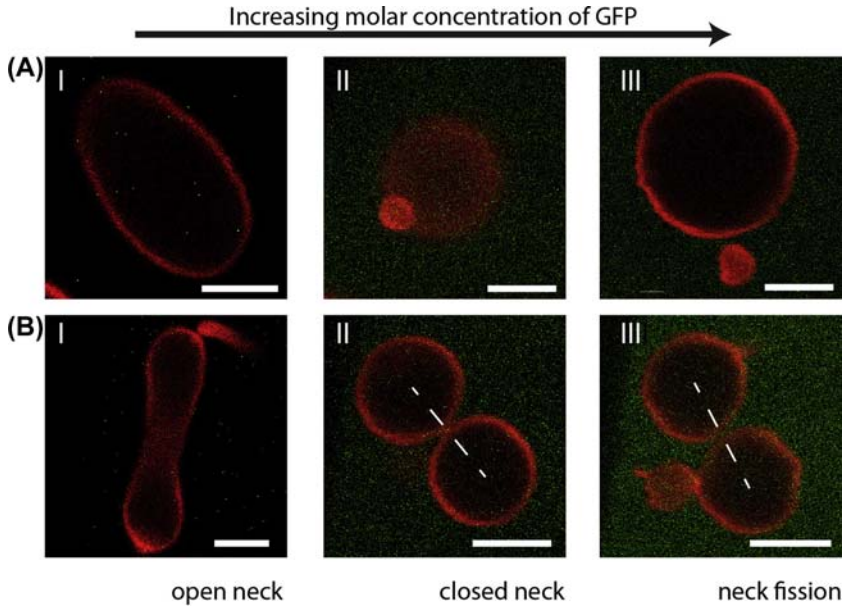


Fig. 17 Division of giant unilamellar vesicles (GUVs) (red) by increasing the molar concentration of green fluorescent protein (GFP) (green) in the exterior aqueous solution: (A) Asymmetric division into one large and one small daughter vesicle; (B) Symmetric division into two daughter vesicles of equal size. The division process starts, in the absence of GFP, from a prolate vesicle shape as displayed in I. Addition of GFP then transforms each GUV into two (punctured) spheres that are connected by a closed membrane neck as in II. A further increase in the GFP concentration leads to the cleavage of the neck and to the division of the GUV as shown in III [5].

directly from two features that we discussed already for the two-sphere shapes and that remain valid for any multisphere shape: (i) the shape equation for spherical segments and (ii) the stability condition for closed membrane necks. The quadratic nature of the shape equation as given by Eq. (47) implies that only up to two different sphere radii can coexist on the same vesicle. Likewise, the local nature of the stability condition for closed membrane necks as given by Eq. (51) ensures that this condition can be applied to the necks of any multispherical shape.

Multispheres with N_l large and N_s small spheres. Thus, let us now consider multispheres built up from N_l large spheres with radius R_l and N_s small spheres with radius R_s . We will focus on morphologies that can be obtained from a spherical vesicle by reducing its volume without changing the area of its membrane. Such a process can be realized by changes in the osmotic conditions, i.e., by osmotic deflation or more complex protocols

involving several deflation and inflation steps. However, we exclude more complex membrane processes such as membrane fusion or fission that change the topology of the vesicle membrane. This topological restriction implies that all spheres of the multispherical shape form linear or branched chains, corresponding to a tree-like topology without cycles. As a consequence, a multisphere that is built up from a total number of $N_{\text{sp}} = N_l + N_s$ spheres is held together by

$$N_{\text{ne}} = N_{\text{sp}} - 1 \text{ necks.} \quad (70)$$

All multispheres that possess such a tree-like topology for a total number of $N_{\text{sp}} \leq 4$ spheres are displayed in Fig. 18.

Inspection of this figure reveals that the different multisphere morphologies with $N_{\text{sp}} \geq 3$ can involve up to two different types of necks while those with $N_{\text{sp}} \geq 4$ can involve up to three different necks. Indeed, a multisphere that is built up from large and small spheres can possess ss-necks

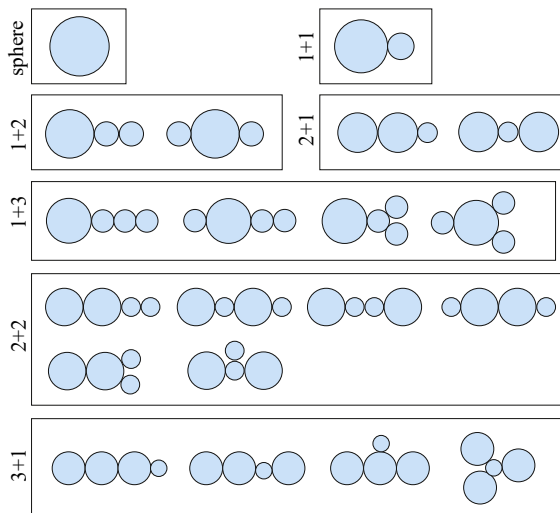


Fig. 18 Multispherical vesicles with N_l large spheres and N_s small spheres up to a total sphere number $N_l + N_s \leq 4$ (for positive sp-curvature). All shapes can be obtained from the spherical vesicle in the upper left corner by reducing the vesicle volume (light blue) for fixed membrane area. Two touching spheres are connected by a closed membrane neck (not shown) that represents a ‘wormhole’ between the two subvolumes. In the examples shown here, the radius R_s of the small spheres is chosen to be half the radius R_l of the large spheres. In general, the radius R_s can vary between $R_s = 1/\sqrt{N_l + N_s}$, corresponding to $N_l + N_s$ equally sized spheres, and $R_s = 0$, corresponding to the limit in which the small spheres are completely taken up by the large spheres.

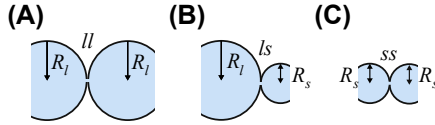


Fig. 19 Different types of membrane necks that can coexist on multispheres built up from a total number of $N_l + N_s \geq 3$ spheres: (A) ll -neck connecting two large spheres with radius R_l ; (B) ls -neck between a large and a small sphere; and (C) ss -neck between two small spheres. The stability of the ss -neck implies the stability of the ls -neck, and the stability of the ls -neck implies the stability of the ll -neck.

connecting two small spheres, ls -necks between one large and one small sphere, as well as ll -necks between two large spheres as displayed in Fig. 19.

Stability relations for different types of necks. To discuss the different necks and their stability, we will first distinguish their neck curvature by introducing the notation

$$M_{ab} \equiv \frac{1}{2} \left(\frac{1}{R_a} + \frac{1}{R_b} \right) \quad (71)$$

where both subscripts a and b can be l or s . Thus, an ll -neck has neck curvature M_{ll} , an ls -neck has neck curvature M_{ls} , and an ss -neck has neck curvature M_{ss} . Because $R_s < R_l$ and $M_s > M_l$, these three neck curvatures are ordered according to

$$M_{ll} < M_{ls} < M_{ss}. \quad (72)$$

The stability condition for a closed neck as given by Eq. (51) now has the form

$$m \geq M_{ab} > 0 \quad \text{with } M_{ab} = M_{ss} \text{ or } M_{ls} \text{ or } M_{ll}. \quad (73)$$

For an ls -neck, we obtain the stability condition $M_{ls} \leq m$ which has the same form as for the single neck of a $(1 + 1)$ -sphere. Likewise, the observation of a stable ss - or ll -neck implies that $m \geq M_{ss} = R_s^{-1}$ and $m \geq M_{ll} = R_l^{-1}$. When a multispherical shape exhibits several types of membrane necks, this shape is only stable if all of its necks are stable against neck opening. Because the neck curvatures are ordered according to $M_{ll} < M_{ls} < M_{ss}$, a sufficiently large spontaneous curvature $m \geq M_{ss}$ ensures that all necks are stable.

Multispheres of GUVs shaped by asymmetric sugar solutions. A striking variety of multispherical shapes has been recently observed experimentally for giant unilamellar vesicles (GUVs) that were exposed to

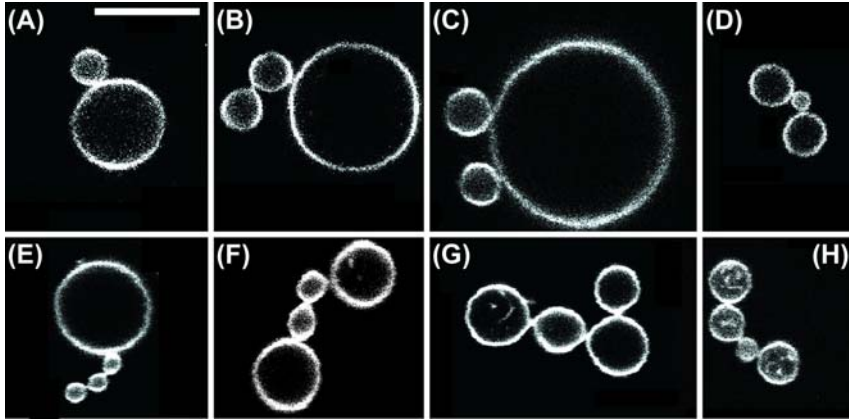


Fig. 20 Multispherical shapes of GUVs built up from N_l large spheres and N_s small spheres with $N_l + N_s \geq 4$ as observed by optical microscopy [6]. These multispheres were formed when the inner and outer leaflets of the GUV membranes were exposed to aqueous sucrose and glucose solutions, respectively. Comparison of the optical images with the cartoons in Fig. 18 shows that many of the possible multisphere morphologies have been observed in these lipid-sugar systems.

asymmetric solutions of two simple sugars, sucrose and glucose [6]. When the interior solution contained only sucrose and the exterior solution primarily glucose, the vesicle membranes acquired a positive spontaneous curvature of about $1\mu\text{m}^{-1}$. Some examples for the resulting multi-sphere morphologies are displayed in Figs. 1B and 20. It is important to note that all of these morphologies involve, to a good approximation, two different radii, R_l and R_s , in agreement with the quadratic nature of the shape Eq. (47). On the one hand, it is quite challenging to obtain images of multispheres in which all spheres have their true radii. Indeed, their apparent radii as seen in the confocal image are typically different from their true radii because the individual spheres move in and out of the optical focus as a result of thermal fluctuations. The true radii are obtained from equatorial cross sections which can be determined by adjusting the focus for each sphere separately but can be rarely seen for all spheres displayed in one image. On the other hand, the observation of such multispherical shape with two different radii provides direct evidence that all spherical membrane segments experience the same mechanical tension and that the whole multisphere is formed by a single bilayer membrane. The experimental observations in Ref. [6] also revealed that the individual spheres are surprisingly mobile and can move along the surface of the multisphere.



10. Summary and outlook

At the end, let me briefly summarize the most interesting results and important developments covered in this review. One important experimental development is certainly the ability to fine-tune the spontaneous curvature by membrane-bound proteins [5]. Using this fine-tuning, we showed that the spontaneous curvature generates a constriction force around the membrane neck of a dumbbell shape [4] by which we can divide the dumbbell-shaped vesicle in a controlled manner. Another important experimental result is the observation of a hydrodynamic instability during the initial aspiration of tubulated GUVs by micropipettes [7]. This instability implies that a GUV with a sufficient amount of membrane area stored in the tubes behaves like a droplet with an effective interfacial tension that is provided by the spontaneous tension. Furthermore, it came as a surprise that aqueous solutions of simple sugars can create a striking variety of multisphere shapes with many membrane necks [6].

When we combine the fine-tuning of the spontaneous curvature with changes in the osmotic conditions to control the vesicle volume, we should be able to study the morphology diagram of giant vesicles in a systematic and quantitative manner. In particular, such studies should provide additional insight into the rugged energy landscape of multisphere shapes. In fact, the experimental studies in Refs. [5,6] provided strong evidence that lipid vesicles with cholesterol exhibit shapes that can be quantitatively described by the spontaneous curvature model. Other intriguing aspects of multispheres that require further studies are their responses to mechanical forces arising from micropipette aspiration, adhesion to other surfaces, or compression by confining walls. In all of these cases, the applied forces will have to overcome certain threshold values to open up the different membrane necks. Once we know how to open and close the membrane necks in a controlled and reliable manner, we will be able to use these multispheres as metamorphic chambers for chemical reactions and nanoparticle growth. Another challenge for future studies is to couple the multispherical vesicles to membrane fission and fusion processes in order to change their topology.

In the context of the molecular simulations, we have extended our mapping between fluid-elastic stress as obtained from the simulations on the molecular level and the two curvature-elastic parameters that can be used to understand the membrane shapes of giant vesicles. We have further corroborated a quantitative relation between the area compressibility and the

bending rigidity [10] which allows us to deduce the bending rigidity with a much lower computational cost. We also realized that it is useful to determine the leaflet tensions and to distinguish tensionless bilayers from tensionless leaflets [9–12], as we did both for planar bilayers and for closed nanovesicles.

The simulations of such nanovesicles revealed a surprising variety of different shapes and shape transformations [12], which could not be observed experimentally because the standard experimental approach is provided by electron microscopy which can provide only a single snapshot of each individual vesicle. So far, our quantitative understanding is restricted to spherical vesicles, for which contributions from area-difference-elasticity can be ignored. When these vesicles transform into nonspherical shapes, area-difference-elasticity should make a significant contribution, which is, however, difficult to determine quantitatively because it is shape-dependent and involves another elastic modulus.

If the molecular bilayer does not contain any lipid species that undergoes flip-flops on the accessible time scales, the number of lipids are conserved or quenched within each leaflet which implies that the leaflet tensions are also conserved for a fixed bilayer geometry. In particular, a tensionless and planar bilayer with $\Sigma = 0$ then leads to two leaflet tensions Σ_{upp} and Σ_{low} with $\Sigma_{\text{low}} = -\Sigma_{\text{upp}}$. However, when we added another flip-flopping lipid species, we observed that the leaflet tensions within the planar bilayers relaxed to zero [11]. Surprisingly, the resulting bilayer with vanishing leaflet tension was observed to possess a significant stress asymmetry and, thus, a significant spontaneous curvature.

It will be rather interesting to study the same relaxation process for spherical nanovesicles, i.e., to find out how the addition of a flip-flopping species changes the stress asymmetry and spontaneous curvature of a spherical nanovesicle. One important issue to address is whether or not we can then obtain a more quantitative comparison with the shapes as obtained from the spontaneous curvature model.

Acknowledgments

I thank all my collaborators for fruitful and enjoyable interactions and the MaxSynBio consortium, jointly funded by the Max Planck Society and Federal Ministry of Research, Germany, for providing a stimulating scientific environment.

References

- [1] R. Lipowsky, E. Sackmann (Eds.), *Structure and Dynamics of Membranes: From Cells to Vesicles*, Handbook of Biological Physics, vol. 1A, Elsevier, Amsterdam, 1995.
- [2] P. Bassereau, P. Sens (Eds.), *Physics of Biological Membranes*, Springer Nature, 2019.
- [3] R. Dimova, C. Marques (Eds.), *The Giant Vesicle Book*, Taylor & Francis, 2019.
- [4] R. Lipowsky, Understanding giant vesicles: a theoretical perspective, in: R. Dimova, C. Marques (Eds.), *The Giant Vesicle Book*, Taylor & Francis, 2019 (Chapter 5).
- [5] J. Steinkühler, R.L. Knorr, T. Bhatia, S. Bartelt, S. Wegner, R. Dimova, R. Lipowsky, Division of cell-sized vesicles controlled by reversible membrane binding of proteins, *Nat. Commun.* (2019) (under revision).
- [6] T. Bhatia, S. Christ, J. Steinkühler, R. Dimova, R. Lipowsky, Morphological complexity of giant vesicles exposed to asymmetric sugar solutions, *Soft Matter* (2019) (page submitted).
- [7] T. Bhatia, J. Agudo-Canalejo, R. Dimova, R. Lipowsky, Membrane nanotubes increase the robustness of giant vesicles, *ACS Nano* 12 (2018) 4478–4485.
- [8] R. Lipowsky, Spontaneous tubulation of membranes and vesicles reveals membrane tension generated by spontaneous curvature, *Faraday Discuss* 161 (2013) 305–331.
- [9] B. Różycki, R. Lipowsky, Spontaneous curvature of bilayer membranes from molecular simulations: asymmetric lipid densities and asymmetric adsorption, *J. Chem. Phys.* 142 (2015) 054101.
- [10] A. Sreekumari, R. Lipowsky, Lipids with bulky head groups generate large membrane curvatures by small compositional asymmetries, *J. Chem. Phys.* 149 (2018) 084901.
- [11] M. Miettinen, R. Lipowsky, Bilayer membranes with frequent flip flops have tensionless leaflets, *Nano Lett.* 19 (2019) 5011–5016.
- [12] R. Ghosh, V. Satarifard, A. Grafmüller, R. Lipowsky, Spherical Nanovesicles transform into a multitude of nonspherical shapes, *Nano Lett.* 19 (2019) 7703–7711.
- [13] P.B. Canham, The minimum energy of bending as a possible explanation of the biconcave shape of the human red blood cell, *J. Theor. Biol.* 26 (1970) 61–81.
- [14] W. Helfrich, Elastic properties of lipid bilayers: theory and possible experiments, *Z. Naturforsch.* 28c (1973) 693–703.
- [15] E.A. Evans, Bending resistance and chemically induced moments in membrane bilayers, *Biophys. J.* 14 (1974) 923–931.
- [16] R. Goetz, G. Gompper, R. Lipowsky, Mobility and elasticity of self-assembled membranes, *Phys. Rev. Lett.* 82 (1999) 221–224.
- [17] W.D. Bancroft, The theory of emulsification, *V. J. Phys. Chem.* 17 (1913) 501–519.
- [18] W.D. Bancroft, C.W. Tucker, Gibbs on emulsification, *J. Phys. Chem.* 31 (1927) 1681–1692.
- [19] F.C. Frank, I. Liquid crystals. On the theory of liquid crystals, *Discuss. Faraday Soc.* 25 (1958) 19–28.
- [20] U. Seifert, K. Berndl, R. Lipowsky, Shape transformations of vesicles: phase diagram for spontaneous curvature and bilayer coupling model, *Phys. Rev. A* 44 (1991) 1182–1202.
- [21] B.W. van der Meer, Fluidity, dynamics, and order, in: M. Shinitzky (Ed.), *Biomembranes: Physical Aspects*, VCH Verlagsgesellschaft, 1993, pp. 97–158.
- [22] J. Liu, J.C. Conboy, 1,2-diacyl-phosphatidylcholine flip-flop measured directly by sum-frequency vibrational spectroscopy, *Biophys. J.* 89 (2005) 2522–2532.
- [23] J. Liu, K.L. Brown, J.C. Conboy, The effect of cholesterol on the intrinsic rate of lipid flip-flop as measured by sum-frequency vibrational spectroscopy, *Faraday Discuss* 161 (2013) 45–61.
- [24] T.L. Steck, J. Ye, Y. Lange, Probing red cell membrane cholesterol movement with cyclodextrin, *Biophys. J.* 83 (2002) 2118–2125.

- [25] J.A. Hamilton, Fast flip-flop of cholesterol and fatty acids in membranes: implications for membrane transport proteins, *Curr. Opin. Lipidol.* 14 (2003) 263–271.
- [26] R.J. Bruckner, S.S. Mansy, A. Ricardo, L. Mahadevan, J.W. Szostak, Flip-flop-induced relaxation of bending energy: implications for membrane remodeling, *Biophys. J.* 97 (2009) 3113–3122.
- [27] R. Lipowsky, From membranes to membrane machines, in: D. Reguera, J.M. Rubi, J.M.B. Vilar (Eds.), *Statistical Mechanics of Biocomplexity, Lecture Notes in Physics*, Springer, Berlin, 1999, pp. 1–23.
- [28] S. Svetina, B. Zeks, Membrane bending energy and shape determination of phospholipid vesicles and red blood cells, *Eur. Biophys. J.* 17 (1989) 101–111.
- [29] L. Miao, U. Seifert, M. Wortis, H.-G. Döbereiner, Budding transitions of fluid-bilayer vesicles: the effect of area-difference elasticity, *Phys. Rev. E* 49 (1994) 5389–5407.
- [30] H.-G. Döbereiner, E. Evans, M. Kraus, U. Seifert, M. Wortis, Mapping vesicle shapes into the phase diagram: a comparison of experiment and theory, *Phys. Rev. E* 55 (4) (1997) 4458–4474.
- [31] U. Seifert, Configurations of membranes and vesicles, *Adv. Phys.* 46 (1997) 13–137.
- [32] R. Lipowsky, H.G. Döbereiner, Vesicles in contact with nanoparticles and colloids, *Europhys. Lett.* 43 (1998) 219–225.
- [33] N. Fricke, R. Dimova, GM1 softens POPC membranes and induces the formation of micron-sized domains, *Biophys. J.* 111 (2016) 1935–1945.
- [34] R. Dimova, Recent developments in the field of bending rigidity measurements on membranes, *Adv. Colloid Interface Sci.* 208 (2014) 225–234.
- [35] P. Bassereau, R. Jin, T. Baumgart, M. Deserno, R. Dimova, V.A. Frolov, P.V. Baskirov, H. Grubmüller, R. Jahn, H.J. Risselada, L. Johannes, M.M. Kozlov, R. Lipowsky, T.J. Pucadyil, W.F. Zeno, J.C. Stachowiak, D. Stamou, A. Breuer, L. Lauritsen, C. Simon, C. Sykes, G. A Voth, T.R. Weikel, The 2018 biomembrane curvature and remodeling roadmap, *J. Phys. D Appl. Phys.* 51 (2018) 343001.
- [36] Y. Liu, J. Agudo-Canalejo, A. Grafmüller, R. Dimova, R. Lipowsky, Patterns of flexible nanotubes formed by liquid-ordered and liquid-disordered membranes, *ACS Nano* 10 (2016) 463–474.
- [37] R. Dasgupta, M.S. Miettinen, N. Fricke, R. Lipowsky, R. Dimova, The glycolipid GM1 reshapes asymmetric biomembranes and giant vesicles by curvature generation, *Proc. Nat. Acad. Sci. USA* 115 (2018) 5756–5761.
- [38] J.A.J. Arpino, P.J. Rizkallah, D.D. Jones, Crystal structure of enhanced green fluorescent protein to 1.35 Å resolution reveals alternative conformations for Glu222, *PLoS One* 7 (10) (2012) e47132.
- [39] Z. Chen, E. Atafi, T. Baumgart, Membrane shape instability induced by protein crowding, *Biophys. J.* 111 (2016) 1823–1826.
- [40] W.T. Snead, C.C. Hayden, A.K. Gadok, C. Zhao, E.M. Lafer, P. Rangamani, J.C. Stachowiak, Membrane fission by protein crowding, *Proc. Nat. Acad. Sci. USA* 114 (2017) E3258–E3267.
- [41] B. Sorre, A. Callan-Jones, J. Manzi, B. Goud, J. Prost, P. Bassereau, A. Roux, Nature of curvature coupling of amphiphysin with membranes depends on its bound density, *Proc. Natl. Acad. Sci.* 109 (1) (2012) 173–178.
- [42] Z.-C. Ou-Yang, W. Helfrich, Bending energy of vesicle membranes: general expressions for the first, second and third variation of the shape energy and applications to spheres and cylinders, *Phys. Rev. A* 39 (1989) 5280–5288.
- [43] R. Lipowsky, Coupling of bending and stretching deformations in vesicle membranes, *Adv. Colloid Interface Sci.* 208 (2014) 14–24.
- [44] H.J. Deuling, W. Helfrich, The curvature elasticity of fluid membranes: a catalogue of vesicle shapes, *J. Physique* 37 (1976) 1335–1345.

- [45] J.S. Rowlinson, B. Widom, *Molecular Theory of Capillarity*, Clarendon Press, Oxford, 1989.
- [46] R. Goetz, R. Lipowsky, Computer simulations of bilayer membranes: self-assembly and interfacial tension, *J. Chem. Phys.* 108 (1998) 7397–7409.
- [47] M. Winterhalter, W. Helfrich, Bending elasticity of electrically charged bilayers: coupled monolayers, neutral surfaces, and balancing stresses, *J. Phys. Chem.* 96 (1992) 327–330.
- [48] R.H. Templer, On the area neutral surface of inverse bicontinuous cubic phases of lyotropic liquid crystals, *Langmuir* 11 (1995) 334–340.
- [49] W. Rawicz, K.C. Olbrich, T. McIntosh, D. Needham, E. Evans, Effect of chain length and unsaturation on elasticity of lipid bilayers, *Biophys. J.* 79 (2000) 328–339.
- [50] J.F. Nagle, Introductory Lecture: basic quantities in model biomembranes, *Faraday Discuss* 161 (2013) 11–29.
- [51] W. Helfrich, Amphiphilic mesophases made of defects, in: R. Balian, et al. (Eds.), *Physics of Defects*, North-Holland Publishing Company, Amsterdam, 1981, pp. 715–755.
- [52] I. Szleifer, D. Kramer, A. Ben-Shaul, W.M. Gelbart, S.A. Safran, Molecular theory of curvature elasticity in surfactant films, *J. Chem. Phys.* 92 (1990) 6800–6817.
- [53] G. Gompper, S. Klein, Ginzburg-Landau theory of aqueous surfactant solutions, *J. Phys. II France* 2 (1992) 1725–1744.
- [54] J.B. Fournier, On the stress and torque tensors in fluid membranes, *Soft Matter* 3 (2007) 883–888.
- [55] M. Deserno, Fluid lipid membranes: from differential geometry to curvature stresses, *Chem. Phys. Lipids* 185 (2015) 11–45.
- [56] B. Różycki, R. Lipowsky, Membrane curvature generated by asymmetric depletion layers of ions, small molecules, and nanoparticles, *J. Chem. Phys.* 145 (2016) 074117.
- [57] T. Nakamura, S. Kawamoto, W. Shinoda, Precise calculation of the local pressure tensor in Cartesian and spherical coordinates in LAMMPS, *Comput. Phys. Commun.* 190 (2015) 120–128.
- [58] V. Satarifard, A. Grafmüller, R. Lipowsky, Nanodroplets at membranes create tight-lipped membrane necks via negative line tension, *ACS Nano* 12 (2018) 12424–12435.
- [59] B. Fourcade, L. Miao, M. Rao, M. Wortis, R.K.P. Zia, Scaling analysis of narrow necks in curvature models of fluid lipid-bilayer vesicles, *Phys. Rev. E* 49 (1994) 5276–5286.
- [60] A. Derzhanski, A.G. Petrov, M.D. Mitov, Molecular asymmetry and saddle-splay elasticity in lipid bilayers, *Ann. Phys.* 3 (1978) 297.
- [61] S. Lorenzen, R.-M. Servuss, W. Helfrich, Elastic torques about membrane edges: a study of pierced egg lecithin vesicles, *Biophys. J.* 50 (1986) 565–572.
- [62] M. Hu, J.J. Briguglio, M. Deserno, Determining the Gaussian curvature modulus of lipid membranes in simulations, *Biophys. J.* 102 (6) (2012) 1403–1410.